

Banner appropriate to article type will appear here in typeset article

Convective mesoscale turbulence at very low Prandtl numbers

Ambrish Pandey^{1†}, Dmitry Krasnov², Katepalli R. Sreenivasan^{1,3,4}, and Jörg Schumacher^{2,3‡}

¹Center for Space Science, New York University Abu Dhabi, PO Box 129188 Abu Dhabi, UAE

²Institut für Thermo- und Fluidodynamik, Technische Universität Ilmenau, PO Box 100565, D-98684 Ilmenau, Germany

³Tandon School of Engineering, New York University, New York NY 11201, USA

⁴Department of Physics and Courant Institute of Mathematical Sciences, New York University, New York, NY 11201, USA

(Received xx; revised xx; accepted xx)

Horizontally extended turbulent convection, termed mesoscale convection in natural systems, remains a challenge to investigate in both experiments and simulations. This is particularly so for very low molecular Prandtl numbers as in stellar convection and in Earth's outer core. The present study reports three-dimensional direct numerical simulations of turbulent Rayleigh-Bénard convection in square boxes of side length L and height H with the aspect ratio $\Gamma = L/H$ of 25, for Prandtl numbers that span almost 4 orders of magnitude, $10^{-3} \leq Pr \leq 7$, and Rayleigh numbers $10^5 \leq Ra \leq 10^7$, obtained by massively parallel computations on grids of up to 5.36×10^{11} points. The low end of this Pr -range cannot be accessed in controlled laboratory measurements. We report the essential properties of the flow and their trends with Rayleigh and Prandtl numbers, in particular the global transport of momentum and heat—the latter decomposed into convective and diffusive contributions—across the convection layer, mean vertical profiles of the temperature and temperature fluctuations, and the kinetic energy and thermal dissipation rates. We also explore the degree to which the turbulence in the bulk of the convection layer resembles classical homogeneous and isotropic turbulence in terms of spectra, increment moments, and dissipative anomaly, and find close similarities. Finally, we show that a characteristic scale on the order of the mesoscale seems to saturate to a wavelength of $\lambda \gtrsim 3H$ for $Pr \lesssim 0.005$. We briefly discuss possible implications of these results for the development of subgrid scale parameterization of turbulent convection.

Key words: Rayleigh-Bénard convection, Low Prandtl number, Dissipative anomaly

[†] Email address for correspondence: ambrish.pandey@nyu.edu

[‡] Email address for correspondence: joerg.schumacher@tu-ilmenau.de

1. Introduction

Thermal convection in stellar and planetary interiors and their atmospheres is complex because it is driven by several factors in combination, but researchers often study the idealized model of convection—the Rayleigh-Bénard convection (RBC)—where a fluid layer bounded between two horizontal plates is heated and cooled uniformly from the bottom and the top, respectively (Tritton 1977; Siggia 1994; Kadanoff 2001; Ahlers *et al.* 2009; Chillà & Schumacher 2012). An important parameter governing RBC is the Prandtl number Pr , which is the ratio of the kinematic viscosity ν and the thermal diffusivity κ of the fluid. Stellar and planetary convection is often characterized by very small Prandtl numbers; for example, $Pr \approx 10^{-6}$ in the Sun (Brandenburg & Subramanian 2005; Schumacher & Sreenivasan 2020; Garaud 2021) and $Pr \approx 10^{-2} - 10^{-1}$ in the Earth’s outer core (Calkins *et al.* 2012; Aurnou *et al.* 2015; Guervilly *et al.* 2019). The Rayleigh number Ra , which characterises the strength of the driving buoyancy force relative to viscous and thermal dissipative forces, is another control parameter, and is very high in most natural flows. The ratio of the horizontal and vertical extents of a convective flow is the aspect ratio Γ ; a crucial feature of all natural convective flows is that $\Gamma \gg 1$, which allows the formation of turbulent superstructures—coherent flow patterns with characteristic scale larger than the depth of the convection layer (Cattaneo *et al.* 2001; Rincon *et al.* 2005). A possible example is supergranulation on Sun’s surface (Nordlund *et al.* 2009; Rincon & Rieutord 2018). Even though RBC incorporates a number of simplifications such as the Boussinesq approximation (Tritton 1977; Schumacher & Sreenivasan 2020), it appears that a study of the flow in extended layers at low Prandtl numbers is highly worthwhile. This is the primary objective of the current work. We are also motivated by the relevance of low- Pr convection for industrial applications that use liquid metals.

Despite this relevance, low- Pr turbulent convection has not been explored extensively in experiments mainly because liquid metals such as mercury, gallium, and sodium are difficult to handle and optically opaque (Cioni *et al.* 1997; Zürner *et al.* 2019). Even when these difficulties are circumvented, the lowest Prandtl number that can be explored is $Pr \approx 0.006$ for liquid sodium (Horanyi *et al.* 1999), which is still some three orders of magnitude higher than in the solar convection zone. Direct Numerical Simulations (DNS) offer important tools but they, too, are hindered by demanding resolution requirements due to the highly inertial nature of low- Pr convection (Breuer *et al.* 2004; Schumacher *et al.* 2015; Scheel & Schumacher 2016, 2017; Pandey *et al.* 2018; Zwirner *et al.* 2020). The fact that the required computational power increases with increasing aspect ratio as Γ^2 further limits numerical investigations. Yet, Pandey *et al.* (2018) were able to perform DNS of RBC in a $\Gamma = 25$ domain by achieving Pr as low as 0.005 at $Ra = 10^5$ to study turbulent superstructures. In the present work, we significantly extend the parameter range from Pandey *et al.* (2018) and Fonda *et al.* (2019) by further decreasing the Prandtl number five-fold, while also increasing the Rayleigh number by two orders of magnitude. The highest Reynolds number achieved in the present work is nearly 5.6×10^4 , requiring massively parallel DNS on computational grids of more than 5×10^{11} points.

This work has three main goals: (1) report trends of heat and momentum transfer with respect to Prandtl number over nearly 4 orders of magnitude; (2) assess the closeness of small-scale statistical properties in the bulk of the convection layer to the classical Kolmogorov-type behaviour (Kolmogorov 1941b; Frisch 1995). This assessment comprises energy spectra, a test of the 4/5-th law and an investigation of the dissipative anomaly (Sreenivasan 1984, 1998) in turbulent convection flow with boundaries; (3) analyse the large-scale circulation patterns, the turbulent superstructures of convection, particularly their trends with decreasing Pr . Note that the convective flows in the Earth’s and stellar interiors are also associated with

(differential) rotation and magnetic fields that can lead to strong departures from local isotropy at larger and intermediate scales (Aurnou *et al.* 2015), but we shall here focus on the influence of low Prandtl number. These DNS series will thus provide a unique data base for the parametrization of turbulent transport in mesoscale configurations characterized by a degree of large-scale order, with well-resolved thermal and kinetic energy dissipation rates.

It is becoming increasingly clear that many properties of low- Pr convective flows differ from those at moderate and high Prandtl numbers. For example, the efficacy of low- Pr flows in transporting heat is lower, and that in transporting momentum higher, than in high- Pr flows; the disparity between the two increases as Pr is lowered (Scheel & Schumacher 2017). Due to high (low) thermal (momentum) diffusivity, low- Pr convection exhibits coarser thermal structures but the length scales in the velocity field have a broader distribution. This results in an enhanced separation between the energy injection and energy dissipation scales in low- Pr convective flows (Schumacher *et al.* 2015). In this regime, the kinetic energy spectrum has been observed to approximate the classical Kolmogorov scaling (Kolmogorov 1941b) with the $-5/3$ power in the inertial range (Mishra & Verma 2010; Lohse & Xia 2010; Bhattacharya *et al.* 2021). Here, we analyse the kinetic energy spectra in the bulk region of the flow and show that it indeed exhibits the classical Kolmogorov scaling with an inertial range, showing no tendency towards Bolgiano scaling (Bolgiano 1959), according to which, the conversion of the kinetic to potential energy leads to the steeper $k^{-11/5}$ scaling in the inertial range (Lohse & Xia 2010; Verma *et al.* 2017; Verma 2018).

Turbulent superstructures of convection can be characterized by a typical spatial scale λ and a temporal scale τ ; finer scales evolve much faster than τ . Thus, the scales λ and τ help distinguish the coarse and gradually evolving large-scale patterns from the finer (and faster) turbulent fluctuations (Pandey *et al.* 2018; Krug *et al.* 2020). The characteristic scales of superstructures have been observed to depend on Pr and Ra (Hartlep *et al.* 2003, 2005; von Hardenberg *et al.* 2008; Bailon-Cuba *et al.* 2010; Emran & Schumacher 2015; Pandey *et al.* 2018; Stevens *et al.* 2018; Schneide *et al.* 2018; Fonda *et al.* 2019; Green *et al.* 2020; Krug *et al.* 2020; Pandey *et al.* 2021; Lenzi *et al.* 2021), as well as on the thermal boundary conditions at the horizontal top and bottom plates (Vieweg *et al.* 2021a). The characteristic length scale of superstructures, which is nearly twice the depth H of the convection layer at the onset of convection, increases with increasing Ra (Stevens *et al.* 2018; Pandey *et al.* 2018). This dependence on Pr is complex, with $\lambda(Pr)$ showing a peak near $Pr \approx 7$ and decreasing as Pr departs from this value (Pandey *et al.* 2018). This decreasing trend of $\lambda(Pr)$ continues to hold up to a $Pr \approx 0.005$ below which the scales seem to level off at a wavelength of $\lambda \gtrsim 3H$.

The remainder of this article is organized as follows. In § 2, we briefly describe the DNS and note the parameter space explored. In § 3, we discuss the flow structures and the scaling of the global transport of heat and momentum, and study in § 4 the vertical profiles of temperature, convective and diffusive transports, as well as dissipation rates. Statistical properties of the flow such as kinetic energy spectra and third-order structure function are examined in § 5 for their compatibility with Kolmogorov forms. The characterisation of turbulent superstructures is presented in § 6. We conclude the main findings in § 7, and present an outlook. Appendices A and B deal with specific tests of sufficient resolution. Appendix C discusses technical detail of the estimates of length and velocity scales of superstructures.

2. Details of direct numerical simulations

We perform direct numerical simulations (DNS) of RBC in a closed rectangular domain with square cross-section of length $L = 25H$, where H is the depth of the convection layer. We solve the following non-dimensionalized equations incorporating the Oberbeck-Boussinesq

(OB) approximation:

$$\frac{\partial \mathbf{u}}{\partial t} + (\mathbf{u} \cdot \nabla) \mathbf{u} = -\nabla p + T \hat{\mathbf{z}} + \sqrt{\frac{Pr}{Ra}} \nabla^2 \mathbf{u}, \quad (2.1)$$

$$\frac{\partial T}{\partial t} + (\mathbf{u} \cdot \nabla) T = \frac{1}{\sqrt{Pr Ra}} \nabla^2 T, \quad (2.2)$$

$$\nabla \cdot \mathbf{u} = 0. \quad (2.3)$$

Here $\mathbf{u} \equiv (u_x, u_y, u_z)$, T , and p are the velocity, temperature and pressure fields, respectively. The Prandtl number Pr and the Rayleigh number $Ra = \alpha g \Delta T H^3 / \nu \kappa$, where α is the coefficient of thermal expansion of the fluid, g is the acceleration due to gravity, and ΔT is the imposed temperature difference between the horizontal plates. We have used the layer's depth H , the free-fall velocity $u_f = \sqrt{\alpha g \Delta T H}$, the free-fall time $t_f = H/u_f$, and ΔT as the non-dimensionalizing length, velocity, time, and temperature scales, respectively. We use the no-slip condition on all boundaries. We employ the isothermal condition on the horizontal plates and the adiabatic condition on the sidewalls. This allows direct comparison with other simulations at higher Pr (Pandey *et al.* 2018; Fonda *et al.* 2019) and controlled laboratory experiments, such as those of Moller *et al.* (2022), in exactly the same setting to enable a consistent analysis across the Ra – Pr parameter plane.

We use two different solvers for the simulations. For moderate and large Pr , we use a spectral element solver NEK5000 (Fischer 1997), where the flow domain is divided into a finite number of elements N_e . The Lagrangian interpolation polynomials of order N are further used to expand the turbulence fields within each element (Scheel *et al.* 2013), thus resulting in a total of $N_e N^3$ mesh cells in the entire flow domain. As low- Pr convection is dominated by inertial forces, the resulting flow acquires increased fine structure whose resolution requires more extensive computational resources (Schumacher *et al.* 2015). Therefore, we performed those simulations using a second-order finite difference solver that requires significantly less working memory at a given grid size. Here, the flow domain is divided into $N_x \times N_y \times N_z$ non-uniform mesh cells (Krasnov *et al.* 2011; Liu *et al.* 2018). We have verified that the results obtained from both the solvers agree well with each other by performing two simulations for $Pr = 0.005$, $Ra = 10^5$ and $Pr = 0.7$, $Ra = 10^7$ using both solvers. We refer to Appendix A for a direct comparison of globally-averaged and horizontally-averaged convective heat fluxes and dissipation rates from the two solvers. Important parameters of all the simulations are provided in table 1.

3. Flow morphology and global transport

3.1. Structures of velocity and temperature fields

Because the time scales of heat and momentum diffusion processes are very different in low- Pr convection, the temperature field shows coarser structures than the velocity field. This is illustrated in figure 1, which displays the instantaneous temperature, vertical velocity, and local turbulent kinetic energy fields in the mid-horizontal plane, $z = H/2$, for the biggest simulations with $Pr = 0.001$, $Ra = 10^7$. The left panels show the fields in the entire cross-section, and the middle and right panels depict the marked magnifications to highlight small-scale structures. The flow pattern of the temperature and vertical velocity fields show similarities at large scales, but the velocity field also consists of very fine structures compared to the highly diffusive temperature field. The finest scale of the turbulent velocity field, denoted as the Kolmogorov scale η , is estimated as $\eta = (\nu^3 / \langle \varepsilon_u \rangle_{V,t})^{1/4}$. Here, $\langle \varepsilon_u \rangle_{V,t}$ is the combined volume-time average of the kinetic energy dissipation rate field per unit mass,

Pr	Ra	No. of mesh cells	$N_{\text{tot}}(\text{bn})$	Nu	Re	u_{rms}	λ/H	$\tau(t_f)$
0.001	10^5	$9600 \times 9600 \times 640$	59	1.21 ± 0.005	4800 ± 30	0.480 ± 0.003	3.12	25
0.005^\dagger	10^5	2367488×11^3	3.1	1.90 ± 0.01	2491 ± 20	0.557 ± 0.001	3.13	22
0.021^\dagger	10^5	2367488×7^3	0.81	2.60 ± 0.01	1120 ± 8	0.513 ± 0.001	3.57	26
0.7^\dagger	10^5	1352000×5^3	0.17	4.26 ± 0.02	92.0 ± 0.4	0.243 ± 0.001	4.14	59
7.0^\dagger	10^5	1352000×5^3	0.17	4.14 ± 0.01	10.7 ± 0.03	0.089 ± 0.001	6.14	214
0.001	10^6	$12800 \times 12800 \times 800$	131	2.48 ± 0.005	19876 ± 1	0.628 ± 0.0001	3.12	19
0.005	10^6	$8192 \times 8192 \times 512$	34	3.52 ± 0.03	7603 ± 20	0.537 ± 0.001	3.57	24
0.021	10^6	$8192 \times 8192 \times 512$	34	4.84 ± 0.01	3157 ± 12	0.457 ± 0.002	4.17	32
0.7^\dagger	10^6	2367488×7^3	0.81	8.10 ± 0.03	290 ± 1	0.242 ± 0.001	4.90	67
$7.0^{\dagger\dagger}$	10^6	2367488×7^3	0.81	8.30 ± 0.02	38.7 ± 0.2	0.102 ± 0.001	6.14	187
0.001	10^7	$20480 \times 20480 \times 1280$	537	4.57 ± 0.01	56256 ± 16	0.562 ± 0.0002	3.57	25
0.7^\dagger	10^7	2367488×11^3	3.1	15.48 ± 0.06	864 ± 3	0.228 ± 0.001	6.3	72
$7.0^{\dagger\dagger}$	10^7	1352000×11^3	1.8	16.25 ± 0.03	130 ± 0.5	0.109 ± 0.001	6.2	138

Table 1: Important parameters of the simulations in a rectangular box of $\Gamma = 25$ with square cross-section; the number of mesh cells, $N_x \times N_y \times N_z$ and $N_e \times N^3$, are for the finite difference and spectral element solvers, respectively; N_{tot} represents the total number of mesh cells in units of a billion; Nu and Re are the volume and time averaged Nusselt and Reynolds numbers, respectively; u_{rms} is the root-mean-square velocity computed over the entire volume; λ and τ are, respectively, the characteristic length and time scales of turbulent superstructures. Runs with superscript \dagger are taken from Pandey *et al.* (2018), while those with superscript $\dagger\dagger$ are taken from Fonda *et al.* (2019).

computed at each point by

$$\varepsilon_u(\mathbf{x}, t) = \frac{\nu}{2} \sum_{i,j=1}^3 \left(\frac{\partial u_i}{\partial x_j} + \frac{\partial u_j}{\partial x_i} \right)^2, \quad (3.1)$$

with u_i representing the velocity component in the direction of coordinate x_i . The finest scale of the temperature field is either the Corrsin scale $\eta_C = \eta/Pr^{3/4}$, which marks the end of the inertial-convective range for $Pr < 1$, or the Batchelor scale $\eta_B = \eta/Pr^{1/2}$, which marks the end of the viscous-convective range for $Pr > 1$; see e.g., Sreenivasan & Schumacher (2010). It is clear that $\eta < \eta_C$ when $Pr < 1$, and $\eta_B < \eta$ when $Pr > 1$. Thus, the finest scales in the flow at hand are either η for $Pr < 1$ or η_B for $Pr > 1$.

The Corrsin scale is nearly 178 times larger than the Kolmogorov scale for $Pr = 0.001$. This large difference is clear in figures 1(c,f), where the temperature and vertical velocity fields are shown in a small cross-section of size $1.56H \times 1.56H$. The figures reveal that the smallest length scale of the thermal structures—the length scale over which the temperature variation is significant—is of the order of H , whereas that for velocity structures is much finer. We also find that the dominant structures in the kinetic energy field resemble those in the vertical velocity because of its dominance in the midplane (Pandey *et al.* 2018). This wide range of length scales present in low- Pr convection engenders a broad inertial range in kinetic energy spectrum, which will be discussed in § 5.2.

To see the effects of Pr on flow structures, we show the temperature and the vertical velocity fields for $Pr = 0.001, 0.7$ and 7 at $Ra = 10^7$ in figure 2. To accentuate small structures, the fields are shown in a quarter (in linear dimension) of the entire cross-section. With increasing Pr , increasingly finer thermal structures are generated due to decreasing thermal diffusivity. On the other hand, the velocity variation becomes progressively regular as the viscosity increases (or the Reynolds number decreases) with increasing Pr .

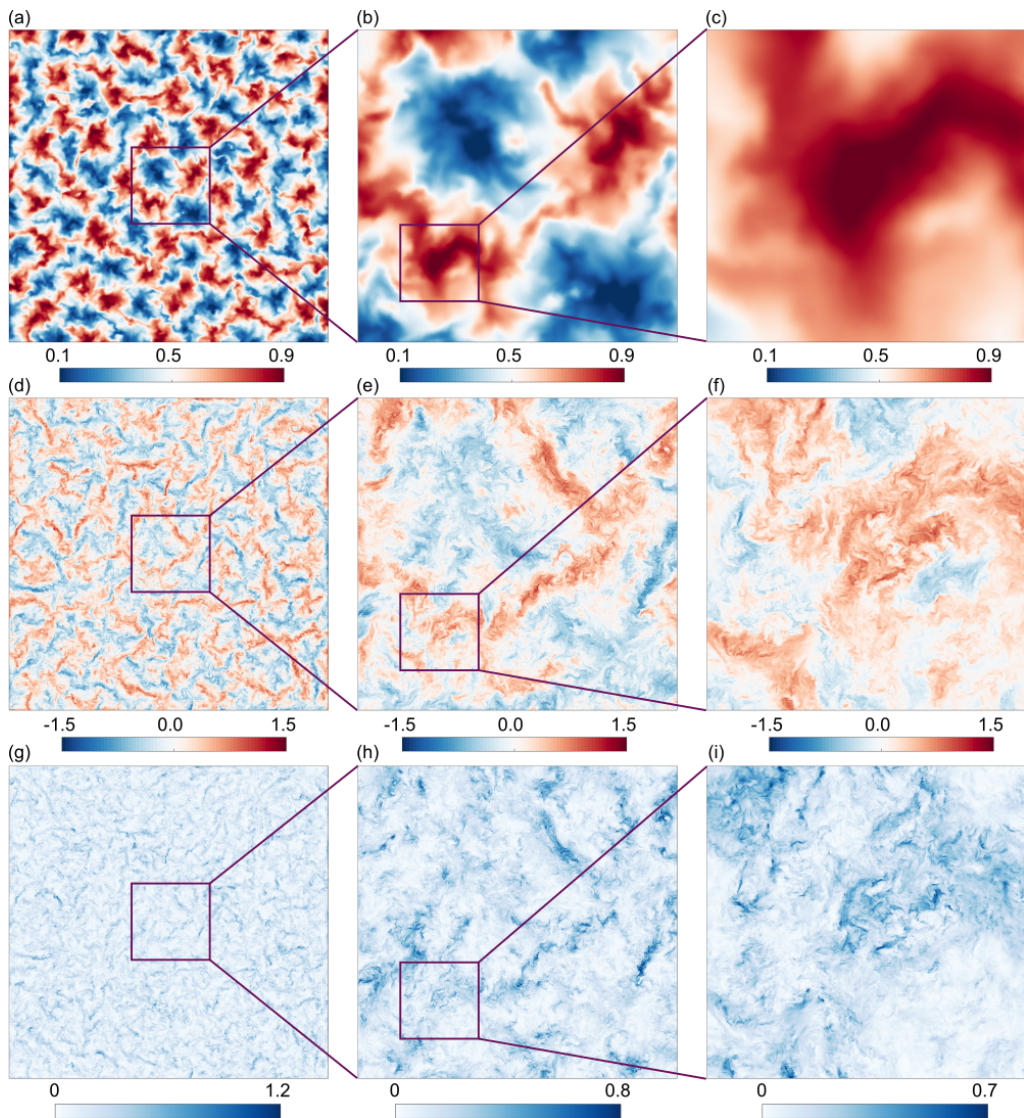


Figure 1: Turbulent superstructures of convection in a low- Pr flow with $Pr = 0.001$ and $Ra = 10^7$. The panels represent instantaneous temperature fields (top row), vertical velocity (middle row), and turbulent kinetic energy in the midplane. In this low- Pr flow, the thermal energy is primarily contained in large-scales, whereas the kinetic energy is distributed over a broad range of scales. Left, middle, and right columns represent fields of view that are $25H \times 25H$, $6.25H \times 6.25H$, and $1.56H \times 1.56H$, respectively.

3.2. Heat and momentum transport laws

Convection at low Prandtl numbers differs from its high- Pr counterpart by reduced heat transport and enhanced momentum transport (Schumacher *et al.* 2015; Scheel & Schumacher 2016, 2017; Pandey *et al.* 2018; Zürner *et al.* 2019; Zwirner *et al.* 2020). Heat transport is quantified by the Nusselt number Nu , defined as the ratio of the total heat transport to that by conduction alone. It is computed as

$$Nu = 1 + \sqrt{RaPr} \langle u_z T \rangle_{V,t}, \quad (3.2)$$

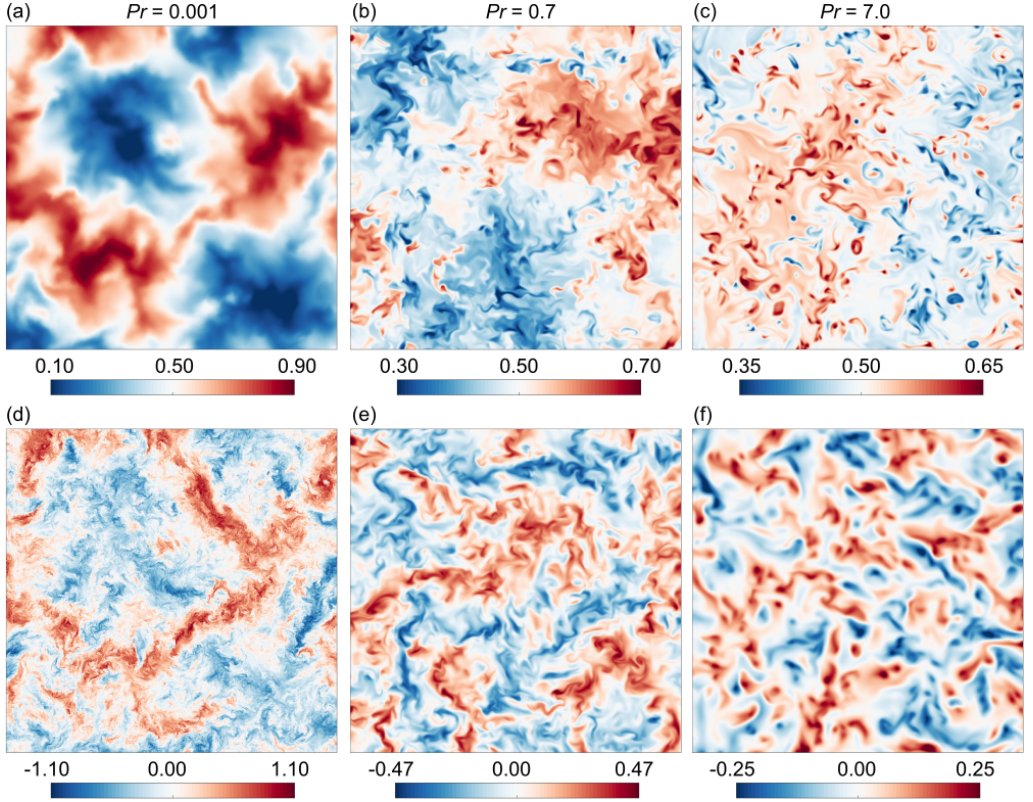


Figure 2: Temperature (top panels) and vertical velocity (bottom panels) in midplane for $Ra = 10^7$. (a,d) are for $Pr = 0.001$, (b,e) for $Pr = 0.7$, and (c,f) for $Pr = 7$. Fields are displayed in a magnified region of dimensions $6.25H \times 6.25H$ around the center. Finer temperature contours can be observed for higher Pr , panel (c), compared to lower Pr , panel (a). The velocity field for lower Pr , panel (d), exhibits much finer structures than those in the other two panels, because the Reynolds number decreases as Pr increases.

where $\langle \cdot \rangle_{V,t}$ denotes again the average over the entire simulation domain and time. We compute Nu for all simulations and plot them, for fixed Ra , as a function of Pr in figure 3(a): Nu increases up to $Pr = 0.7$ but does not change significantly thereafter. A similar trend has also been reported in literature for convection in $\Gamma \approx 1$ domains (Verzicco & Camussi 1999; Schmalzl *et al.* 2004; van der Poel *et al.* 2013) and also for $\Gamma = 0.1$ (Pandey & Sreenivasan 2021). Figure 3(a) indicates that the molecular diffusion becomes an increasingly dominant mode of heat transport as Pr decreases. For $Ra = 10^5$ and 10^6 , we do best fits to the data for $Pr \leq 0.7$. The transport laws $Nu(Pr)$ for both Rayleigh numbers are given, including error bars, in table 2. In summary, we find that the Nusselt number is consistent with the power law $Nu \sim Pr^{0.19}$ for $Ra = 10^5$ and $Nu \sim Pr^{0.18}$ for $Ra = 10^6$. These power law exponents in the extended convection domain are within the range observed in RBC with $\Gamma \lesssim 1$, as shown in Pandey & Sreenivasan (2021), where more discussion of the $Nu - Pr$ scaling exponent can be found.

Normalized values of global heat transport in RBC increases with increasing thermal driving and the rate of increase depends on the Prandtl number (Scheel & Schumacher 2016, 2017). We plot Nu for $Pr = 0.001, 0.7$, and 7 against Ra in figure 3(b), which shows that Nu for $Pr = 0.7$ and 7 are nearly similar. There are only three data points, which would not be adequate to establish a new result. Nevertheless, power-law fits to those three points

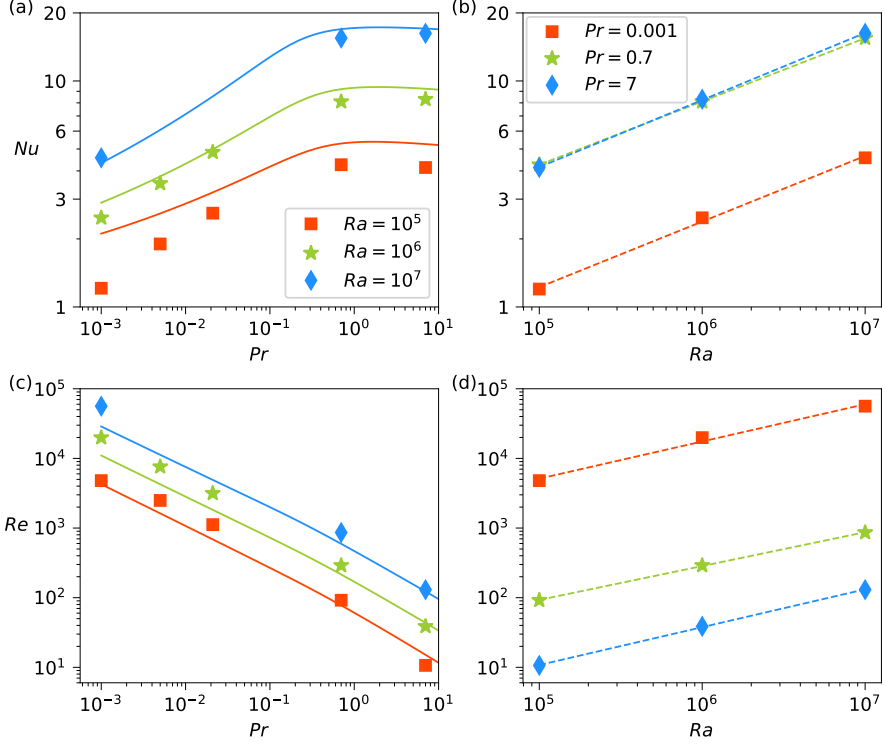


Figure 3: (a) Nusselt number for $\Gamma = 25$ increases with increasing Pr for low Prandtl numbers but does not change much for $Pr \geq 0.7$, consistent with Pandey & Sreenivasan (2021). (b) Nu as a function of Ra increases approximately as $Ra^{0.29}$. (c) The Reynolds number based on the root-mean-square velocity decreases with increasing Pr , with power law exponents consistent with others in the literature. (d) Re as a function of Ra increases as $Ra^{0.5}$ for all the three cases. The dashed lines in panels (b) and (d) are best fits, summarized in table 2. Solid lines in panels (a, c) are predictions of Nu and Re from the Grossmann-Lohse theory. Legends in top panels also apply to the corresponding bottom panels.

serve to supplement existing results. We obtain approximately $Nu \sim Ra^{0.29}$ (see table 2). The exponents for all the three Prandtl numbers are essentially similar and agree with those observed in convection for $\Gamma \sim 1$ (Bailon-Cuba *et al.* 2010; Stevens *et al.* 2011; Scheel *et al.* 2012; Scheel & Schumacher 2014, 2016). It is interesting that the exponent for $Pr = 0.001$ is not lower compared to that for $Pr \geq 0.7$. A slightly lower scaling exponent of 0.27 ± 0.01 was reported from simulations in closed cylinders for $\Gamma = 1$ (Scheel & Schumacher 2017) at $Pr = 0.021$. Recent experiments in strongly turbulent liquid metal convection by Schindler *et al.* (2022), at nearly the same Prandtl number but for Rayleigh numbers up to $Ra = 5 \times 10^9$, in a cylinder with $\Gamma = 1/2$, reported an even smaller scaling exponent of 0.124. It is possible that the constrained large-scale flow in closed cylinder affects the scaling exponent at low and moderate Rayleigh numbers, see discussion by Pandey & Sreenivasan (2021).

The Reynolds number Re quantifies the momentum transport in RBC. We compute it with H and u_{rms} as the relevant length and velocity scales, as

$$Re = u_{\text{rms}} \sqrt{\frac{Ra}{Pr}} \quad \text{where} \quad u_{\text{rms}} = \sqrt{\langle u_i^2 \rangle_{V,t}}. \quad (3.3)$$

is the root-mean-square (rms) velocity. The Reynolds number as a function of Pr is plotted

Ra	Pr	Nu	Re
10^5	$0.001 - 0.7$	$(4.8 \pm 0.2)Pr^{0.19 \pm 0.02}$	$(84 \pm 9)Pr^{-0.62 \pm 0.05}$
10^6	$0.001 - 0.7$	$(9.0 \pm 0.3)Pr^{0.18 \pm 0.01}$	$(240 \pm 8)Pr^{-0.65 \pm 0.02}$
$10^5 - 10^7$	0.001	$(0.043 \pm 0.004)Ra^{0.29 \pm 0.01}$	$(10.9 \pm 3.1)Ra^{0.53 \pm 0.05}$
$10^5 - 10^7$	0.7	$(0.17 \pm 0.001)Ra^{0.28 \pm 0.001}$	$(0.34 \pm 0.02)Ra^{0.49 \pm 0.01}$
$10^5 - 10^7$	7	$(0.14 \pm 0.003)Ra^{0.30 \pm 0.003}$	$(0.021 \pm 0.001)Ra^{0.54 \pm 0.01}$

Table 2: Summary of scaling relations for global heat and momentum transports as functions of Ra and Pr . Note that the scaling laws with respect to Ra have been obtained by fits to 3 data points only; it is clear that more definitive results require larger number of data points.

in figure 3(c), which reveals that, for fixed Ra , the flow loses its effectiveness in transporting momentum as Pr increases (Käpylä 2021). In thermal convection, the power law exponent of $Re - Pr$ scaling depends on the range of Pr ; the Reynolds number decreases with increasing Pr even when the flow is dominated by inertia. The detailed power law fits can be found in table 2. As a summary, we get $Re \sim Pr^{-0.62}$ and $Re \sim Pr^{-0.65}$ for $Ra = 10^5$ and $Ra = 10^6$, respectively. As for the Nusselt number, the exponents of the $Re - Pr$ scaling agree with those observed for $\Gamma \lesssim 1$ (Verzicco & Camussi 1999; Pandey & Sreenivasan 2021).

The Reynolds number variation with Ra , plotted in figure 3(d), shows that Re is consistently higher for lower Prandtl numbers, manifesting in the enhanced prefactors of the power law fits which are summarized in table 2. The best fits yield $Re \sim Ra^{0.53}$, $Re \sim Ra^{0.49}$, and $Re \sim Ra^{0.54}$ for $Pr = 0.001, 0.7$, and 7 , respectively. Note that the Reynolds number based on the free-fall velocity scales as $Ra^{0.50}$. Thus, these scaling exponents suggest that the free-fall velocity for a fixed Pr does not depend strongly on Ra (see table 1). The scaling exponents are in the same range as in several other studies in the past; the exponent does not, however, decrease with decreasing Prandtl number as found by Scheel & Schumacher (2017). This might be the result of differences in the aspect ratio, but we reiterate that the present fits use only 3 data points.

Attempts have been made to predict the global transports in RBC as a function of the control parameters (Shraiman & Siggia 1990; Grossmann & Lohse 2000; Pandey & Verma 2016). Grossmann & Lohse (2000) assumed the existence of a large-scale circulation of the order of the size of the convection cell, and proposed a set of coupled equations relating Nu and Re as functions of Ra and Pr (Grossmann & Lohse 2001). The equations also include a set of constant coefficients, whose values depend on the aspect ratio of the domain. Using the coefficients provided in Stevens *et al.* (2013) for $\Gamma \approx 1$ RBC, we compute Nu as a function of Pr from the Grossmann-Lohse model and show them as solid curves in figure 3(a). The Nusselt numbers thus estimated are somewhat higher than those computed from the DNS for $Ra = 10^5$. On the low- Pr end, this may be attributed to the fact that the temperature fields for these parameter pairs are dominated by diffusion and barely mixed in the bulk. However, the agreement is better for $Ra \geq 10^6$, which indicates that the heat transport in our extended cell is not much different from that in $\Gamma = 1$ cells. We also plot $Re(Pr)$ from the Grossmann-Lohse model in figure 3(c), and find that there is fair agreement; see also Verma (2018).

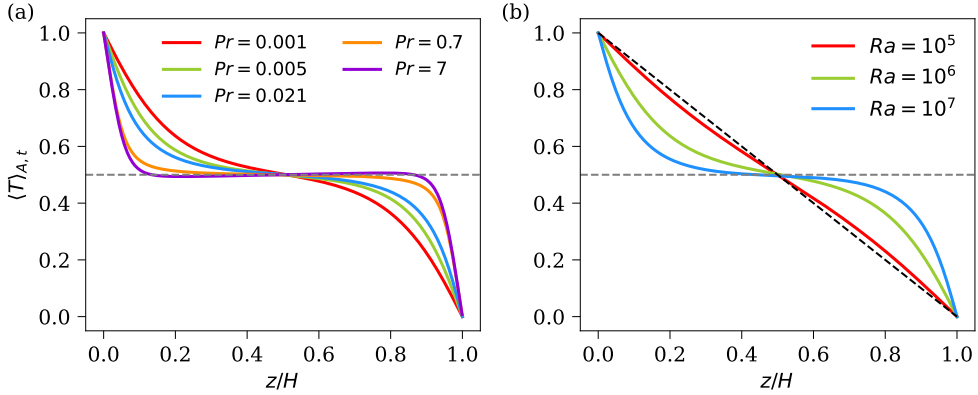


Figure 4: Horizontal and time averages of temperature as a function of the depth for simulations at (a) $Ra = 10^6$ and (b) $Pr = 0.001$. A well-mixed isothermal region away from the walls occurs only for $Pr \geq 0.7$ in (a), whereas a significant temperature gradient in the central region occurs for lower Pr . Dashed black line in panel (b) corresponds to the dimensionless conduction temperature profile $T_{\text{cond}} = 1 - z$.

4. Vertical profiles across the convection layer

4.1. Temperature and heat flux fields

In the conductive equilibrium state, the vertical temperature gradient is a constant; inhomogeneities in the horizontal directions arise in the convective state, leading to a modification of the linear temperature profile. We compute the mean temperature profile $\langle T \rangle_{A,t}(z)$ and plot them in figure 4. Here, $\langle \cdot \rangle_{A,t}$ stands for the averaging over the entire horizontal cross-section of $A = 25H \times 25H$ at a fixed height z and the full time interval. In a turbulent convective flow, almost the entire temperature drop occurs within the thermal boundary layers (BLs) on the horizontal plates, while the bulk of the flow outside these BLs remains nearly isothermal (and thus well-mixed). Figure 4(a) exhibits this feature. However, the slope of the temperature profile in the midplane increases as Pr decreases. We plot the profiles for $Pr = 0.001$ for all the Rayleigh numbers in figure 4(b). The profile for $Ra = 10^5$ departs only weakly from the linear conduction profile despite a high Reynolds number of the flow. The temperature gradient in the central plane decreases with increasing Ra , and even a Rayleigh number of 10^7 is not enough to generate a well-mixed temperature field in the bulk region for this very low Pr .

In OB convection, the temperature averaged over the entire flow domain is $\Delta T/2$ but fluctuates at each point in the flow. We decompose the temperature field into its mean and fluctuation as

$$T(\mathbf{x}, t) = \langle T \rangle_{A,t}(z) + \theta(\mathbf{x}, t). \quad (4.1)$$

Even though the temperature field becomes increasingly diffusive as Pr decreases, the fluctuations increase with decreasing Pr ; see figure 5(a) for $Ra = 10^7$. The depth variation is captured by the planar temperature fluctuation computed as

$$\theta_{\text{rms}}(z) = \sqrt{\langle [T - \langle T \rangle_{A,t}(z)]^2 \rangle_{A,t}} = \sqrt{\langle T^2(z) \rangle_{A,t} - \langle T(z) \rangle_{A,t}^2}. \quad (4.2)$$

Figure 5(a) shows that $\theta_{\text{rms}}(z)$ vanishes at the plate due to the imposed isothermal boundary condition. With increasing distance from the bottom plate, however, the strength of fluctuations increases within the thermal BL region. The maxima in $\theta_{\text{rms}}(z)$ profiles occur near the edge of the thermal BL (computed as $0.5H/Nu$) marked as dashed vertical lines in figure 5(a).

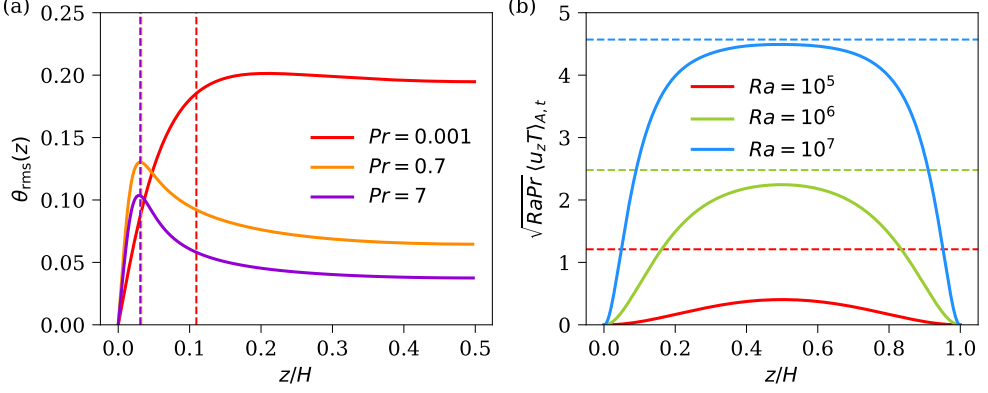


Figure 5: (a) Root-mean-square temperature fluctuation profiles averaged over the top and bottom halves varying with the distance from the plate for $Ra = 10^7$. The peaks in $\theta_{\text{rms}}(z)$ occur near the thermal BL edge, which are indicated by dashed vertical lines. (b) Vertical profiles of the convective heat flux for $Pr = 0.001$. Dashed horizontal lines indicate the global heat flux (Nu) for each case. The convective flux vanishes at the top and bottom plates and is largest in the central plane.

This suggests that the thermal plumes retain their temperature, while the temperature of the ambient fluid decreases (increases) with increasing distance from the bottom (top) plate. This leads to an increasing contrast between the two components of the flow and is reflected as an increasing $\theta_{\text{rms}}(z)$ within the BL region (Pandey 2021). In the bulk region, however, θ_{rms} decreases with distance from the plate because the plumes do not retain their identity and begin to mix with the bulk fluid.

The heat transport occurs due to convective as well as diffusive processes, with their ratio varying with depth. To get the total heat flux in a horizontal plane, we average the temperature equation (2.2) in horizontal directions and in time, which leads to

$$Nu(z) = \sqrt{RaPr} \langle u_z T \rangle_{A,t} - \frac{\partial \langle T \rangle_{A,t}}{\partial z} = \text{const}. \quad (4.3)$$

It is clear from the temperature profiles in figure 4 that the diffusive contribution $-\partial \langle T \rangle_{A,t} / \partial z$ should be small in the well-mixed bulk region—increasing towards the plates and becoming largest at the plates. The variation of the convective heat flux $\sqrt{RaPr} \langle u_z T \rangle_{A,t}$ with depth in figure 5(b) for $Pr = 0.001$ confirms this expectation. The magnitudes of the globally-averaged heat flux are indicated as dashed horizontal lines in figure 5(b), showing that the diffusive flux (the distance between the solid curves and the corresponding dashed horizontal lines) is not negligible even in the central region for $Ra \leq 10^6$. The diffusive component dominates the total heat flux in the central region for $Ra = 10^5$, which is consistent with the highly inefficient convective heat transport; see table 1. However, for $Ra = 10^7$, the diffusive contribution diminishes in the central plane. Thus, as Pr becomes smaller, one requires increasing Ra before turbulent processes become important.

4.2. Thermal and kinetic energy dissipation rates

While the mean temperature $\langle T \rangle_{A,t}(z)$ varies sharply near the horizontal plates and weakly in the central region, the vertical mean profile of the thermal dissipation rate field, which is

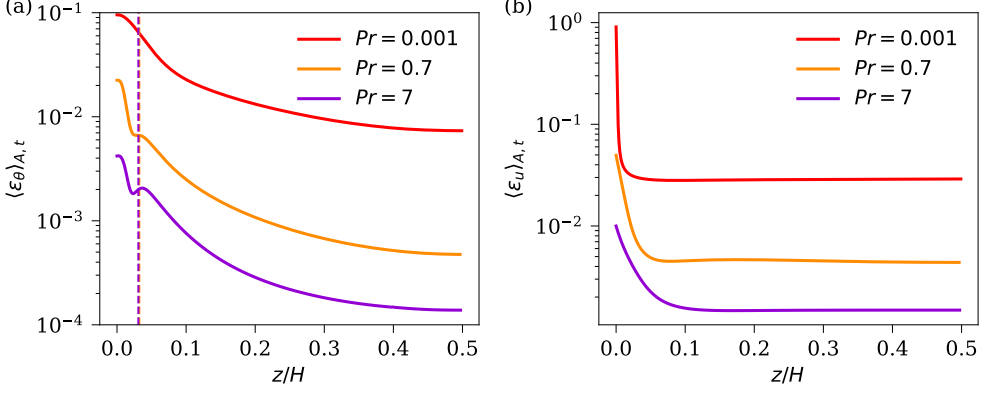


Figure 6: Variation of the horizontally averaged (a) thermal and (b) kinetic energy dissipation rates in the vertical direction for $Ra = 10^7$. The profiles are further averaged over the top and bottom halves of the domain to improve the statistics. The dissipation profiles are largest at the plates and decrease towards the central plane; however, the $\varepsilon_u(z)$ is nearly uniform in the bulk region. The (indistinguishable) dashed vertical lines in panel (a) indicate the edges of the thermal BLs for $Pr = 0.7$ and $Pr = 7$.

the rate of loss of thermal variance that is computed pointwise by

$$\varepsilon_T(\mathbf{x}, t) = \kappa \left[\left(\frac{\partial T}{\partial x} \right)^2 + \left(\frac{\partial T}{\partial y} \right)^2 + \left(\frac{\partial T}{\partial z} \right)^2 \right], \quad (4.4)$$

is higher in the vicinity of the horizontal plates and decreases towards the centre (Scheel & Schumacher 2016). We also compute the thermal dissipation rate field defined as

$$\varepsilon_\theta(\mathbf{x}, t) = \kappa \left[\left(\frac{\partial \theta}{\partial x} \right)^2 + \left(\frac{\partial \theta}{\partial y} \right)^2 + \left(\frac{\partial \theta}{\partial z} \right)^2 \right] \quad (4.5)$$

to quantify the spatial variation of the temperature fluctuations. The mean profile of the thermal dissipation rate $\langle \varepsilon_\theta \rangle_{A,t}(z)$ is plotted in figure 6(a) for $Ra = 10^7$. Note that the vertical mean profiles of ε_T and ε_θ are related by

$$\langle \varepsilon_T \rangle_{A,t}(z) = \langle \varepsilon_\theta \rangle_{A,t}(z) + \varepsilon_{\langle T \rangle}(z), \quad (4.6)$$

where $\varepsilon_{\langle T \rangle} = \kappa(d\langle T \rangle_{A,t}/dz)^2$ is the dissipation rate corresponding to the mean temperature profile (Emran & Schumacher 2008). In convective flows with well-developed thermal BLs, $\varepsilon_{\langle T \rangle}$ contributes primarily to the boundary layers and negligibly in the bulk. This rapid decrease of $\varepsilon_{\langle T \rangle}$ outside the thermal BL region shows a shallow kink in the profiles of $\langle \varepsilon_\theta \rangle_{A,t}(z)$. In figure 6(a), we indicate the thermal BL thicknesses for $Pr = 0.7$ and $Pr = 7$ as dashed vertical lines, and note that the kinks are observed near the edge of the thermal BL. The kink does not appear for $Pr = 0.001$ due to the absence of well-developed thermal BLs.

We find that $\langle \varepsilon_\theta \rangle_{A,t}(z)$ increases with decreasing Pr . This is because the volume-averaged thermal dissipation rate is related to the global heat transport (Shraiman & Siggia 1990) as

$$\langle \varepsilon_T \rangle_{V,t} = \frac{Nu}{\sqrt{RaPr}}. \quad (4.7)$$

As we observe $Nu \sim Pr^{0.2}$, this leads to $\langle \varepsilon_T \rangle_{V,t} \sim Pr^{-0.3}$ for a fixed Ra . Thus, the decrease of the thermal dissipation rate with increasing Pr is consistent with the Pr -dependence of the Nusselt number.

z/H	(Ra, Pr)	(Ra, Pr)	(Ra, Pr)	(Ra, Pr)	(Ra, Pr)
	$10^5, 0.001$	$10^6, 0.001$	$10^7, 0.001$	$10^6, 0.005$	$10^6, 0.021$
0.5	0.971	0.980	0.957	0.953	0.963
0.1	1.132	1.008	1.018	1.056	1.173
0.01	11.35	3.225	1.657	7.108	12.51

Table 3: The anisotropy coefficient G_{11} in three horizontal planes; for definition see (5.1). G_{11} as well as the other coefficients G_{ij} remain close to unity in the bulk region between $z = 0.1H$ and $z = 0.9H$, but depart significantly as the horizontal plate is approached and the shear effects dominate.

We now plot in figure 6(b) the profiles of the viscous dissipation rate defined in (3.1). Similar to $\langle \varepsilon_\theta \rangle_{A,t}(z)$, the largest values of $\langle \varepsilon_u \rangle_{A,t}(z)$ are found near the horizontal plate owing to the strongly varying velocity field in the vicinity of the plates. Further, the variation of the profiles $\langle \varepsilon_u \rangle_{A,t}(z)$ in the bulk region is almost negligible compared to that in the viscous BL region near the plates. Figure 6(b) shows that $\langle \varepsilon_u \rangle_{A,t}(z)$ increases with decreasing Pr for all z . Note that the globally-averaged viscous dissipation rate is related to the Nusselt number as

$$\langle \varepsilon_u \rangle_{V,t} = \frac{Nu - 1}{\sqrt{RaPr}}, \quad (4.8)$$

and therefore, $\langle \varepsilon_u \rangle_{V,t}$ should decrease with increasing Pr .

5. Characterization of the turbulence in the bulk

5.1. Isotropy in the midplane

Vorobev *et al.* (2005) used the ratios

$$G_{ij} = \frac{\langle (\partial u_i / \partial z)^2 \rangle (1 + \delta_{iz})}{\langle (\partial u_i / \partial x_j)^2 \rangle (1 + \delta_{ij})} \quad \text{with } i, j = x, y, z \quad (5.1)$$

to determine the degree of anisotropy on the level of second-order derivative moments. Flows with no variation in the vertical direction z yield $G_{ij} \rightarrow 0$ (and are thus anisotropic), while $G_{ij} = 1$ for perfectly isotropic flows. The coefficient G_{11} , relating the in-plane derivative to a transverse derivative with respect to the vertical direction is summarized in three horizontal planes in table 3. G_{11} remains nearly unity in the bulk region for $0.1 \leq z/H \leq 0.9$, but significant departures are found near the horizontal plates. Similar amplitudes follow for other combinations; see also Nath *et al.* (2016). We thus conclude that a plausible case exists for exploring similarities with Kolmogorov turbulence in the bulk region; see Mishra & Verma (2010) and Verma *et al.* (2017).

5.2. Kinetic energy spectra

In three-dimensional turbulent flows, the kinetic energy injected at large length scales cascades towards smaller scales and eventually gets dissipated at the smallest scales by viscous action.[†] In the inertial range—the range of length scales far from both the injection as well as dissipation scales—the kinetic energy spectrum $E(k)$, whose integral over all wavenumbers k yields the kinetic energy, follows the standard Kolmogorov scaling

$$E(k) = K_K \varepsilon_u^{2/3} k^{-5/3}, \quad (5.2)$$

[†] We shall not consider the connection to the Onsager conjecture that it may be related to singularities in weak solutions of the Euler equations.

where K_K is the Kolmogorov constant and ε_u denotes the volume- and time-averaged kinetic energy dissipation rate.

For our purposes, it would be useful to study the behaviour of two-dimensional (2D) energy spectrum in a horizontal plane. The 2D Fourier transform of a field $f(x, y, z_0)$ in a horizontal plane at $z = z_0$ is defined as

$$f(x, y, z_0) = \int_{-\infty}^{\infty} \int_{-\infty}^{\infty} \hat{F}(k_x, k_y) e^{-i(k_x x + k_y y)} dk_x dk_y, \quad (5.3)$$

where $\hat{F}(k_x, k_y)$ is the Fourier mode corresponding to the wavevector $\mathbf{k} \equiv (k_x, k_y)$. Thus, the Fourier modes of the velocity field in midplane $\mathbf{u}(x, y, z = H/2) \equiv \mathbf{U}(x, y)$ are denoted as $\hat{\mathbf{U}}(\mathbf{k}) \equiv [\hat{U}_x(\mathbf{k}), \hat{U}_y(\mathbf{k}), \hat{U}_z(\mathbf{k})]$. The kinetic energy in a horizontal plane is equal to the sum of the energies of each Fourier mode, i.e.,

$$\begin{aligned} \frac{1}{2} \langle \mathbf{U}^2 \rangle_{A,t} &= \int_{-\infty}^{\infty} \int_{-\infty}^{\infty} \frac{1}{2} |\hat{\mathbf{U}}(k_x, k_y)|^2 dk_x dk_y \\ &= \int_0^{\infty} \left[\int_0^{2\pi} \frac{1}{2} |\hat{\mathbf{U}}(k, \phi_k)|^2 d\phi_k \right] k dk, \end{aligned} \quad (5.4)$$

with

$$k = \sqrt{k_x^2 + k_y^2} \quad \text{and} \quad \phi_k = \arctan(k_y, k_x). \quad (5.5)$$

Using the horizontal isotropy of the fields, the expression in the square brackets could be readily integrated to yield $\pi |\hat{\mathbf{U}}(k)|^2$, where $|\hat{\mathbf{U}}(k)|^2/2$ is the average kinetic energy of all the Fourier modes lying in an annular region between radii k and $k + dk$. Thus, the average planar kinetic energy becomes

$$\frac{1}{2} \langle \mathbf{U}^2 \rangle_{A,t} = \int_0^{\infty} \pi k |\hat{\mathbf{U}}(k)|^2 dk = \int_0^{\infty} E(k) dk, \quad (5.6)$$

where $E(k) = \pi k |\hat{\mathbf{U}}(k)|^2$ is the one-dimensional (1D) kinetic energy spectrum in a horizontal plane (Peltier *et al.* 1996).

We compute the energy spectrum in the midplane of the low- Pr flows for each instantaneous snapshot and then average the instantaneous spectra over all the available snapshots to obtain the mean kinetic energy spectrum. The energy spectra for flows with small-scale universality at different Reynolds numbers should collapse at sufficiently high Reynolds number if they are plotted against $k\eta$. Equation (5.2) in terms of the normalized wavenumber $k\eta$ reads then (Monin & Yaglom 2007) as

$$E(k\eta) = K_K (\varepsilon_u \nu^5)^{1/4} (k\eta)^{-5/3}. \quad (5.7)$$

We now plot the normalized energy spectra $E(k\eta)(\varepsilon_u \nu^5)^{-1/4}$ as a function of $k\eta$ in figure 7. The spectra for $Pr = 0.001$ are shown in figure 7(a) for all three Rayleigh numbers, whereas the spectra for a fixed $Ra = 10^6$ and $Pr = 0.001, 0.005$, and 0.021 are displayed in figure 7(b). The collapse is excellent beyond the wavenumber corresponding to the maximum of $E(k\eta)$. We show the same spectra in the normalized form $E(k)\varepsilon_u^{-2/3}k^{5/3}$ in the insets of figure 7, which confirm that they collapse on each other for all the low- Pr flows in low to moderately large wavenumber range. The plateau in the dimensionless wavenumber range $k \in [k_0, k_1]$ increases with increasing Ra . The inset of figure 7(a) shows that the inertial range $[k_0, k_1]$ can be estimated to be $[2, 60]$, $[4, 150]$, and $[6, 300]$ for $Ra = 10^5, 10^6, 10^7$ and $Pr = 0.001$, respectively. The inertial range increases with increasing Ra and decreasing Pr , as expected from the increased Reynolds numbers.

The energy spectra normalized in the same way for $Pr = 0.001, 0.005$, and 0.021 for a fixed

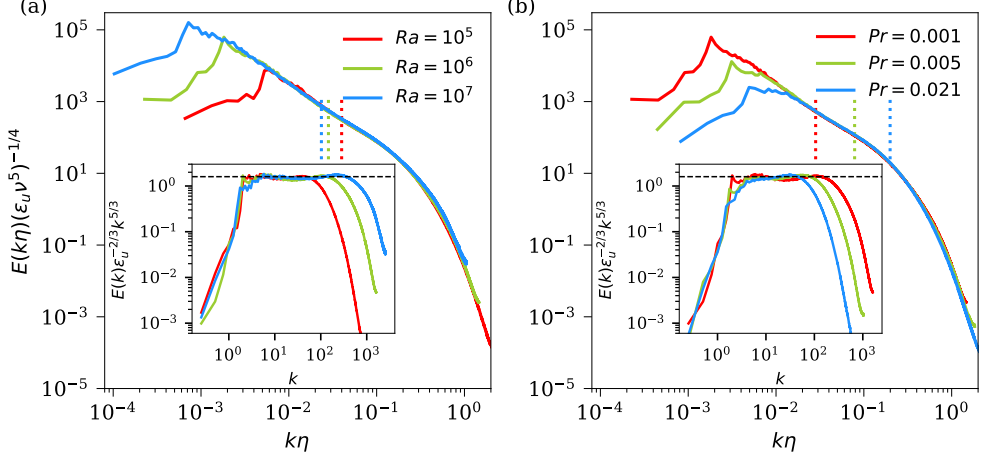


Figure 7: Normalized kinetic energy spectra $E(k\eta)(\varepsilon_u \nu^5)^{-1/4}$ in the midplane as a function of the normalized wavenumber $k\eta$ for $Pr = 0.001$ (a) and $Ra = 10^6$ (b) collapse well in the inertial as well as viscous ranges. Here, $\varepsilon_u = \langle \varepsilon_u \rangle_{V,t}$. The short dotted vertical lines indicate the normalized wavenumber $k_T \eta$, where $k_T = 2\pi/\delta_T$ is the wavenumber corresponding to the mean thermal boundary layer thickness $\delta_T = H/(2Nu)$. Insets show that the corresponding spectra normalized with $\varepsilon_u^{2/3} k^{-5/3}$ exhibit plateau in the inertial range, which becomes wider with increasing Ra or decreasing Pr . The dashed horizontal line in the insets yields the Kolmogorov constant $K_K \approx 1.6$ in the planar energy spectra, consistent with the value for isotropic turbulence (Sreenivasan 1995).

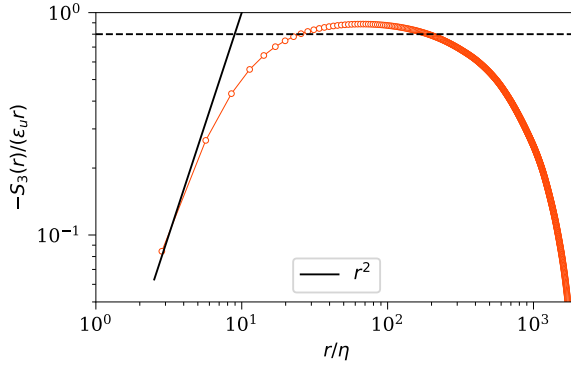


Figure 8: Third-order longitudinal structure function (averaged over the x - and y -directions) in the midplane for $Pr = 0.001, Ra = 10^7$ varies as r^2 in the viscous range, whereas it remains nearly a constant in the inertial range. Dashed horizontal line indicates the constant $4/5$ appearing in equation (5.10). Here, $\varepsilon_u = \langle \varepsilon_u \rangle_{A,t} (z = H/2)$.

$Ra = 10^6$ are shown in the inset of figure 7(b). Again, the normalized spectra collapse quite well. A plateau can be detected for the two lower Pr with the inertial range corresponding to $[4, 150]$ and $[4, 90]$ for $Pr = 0.001$ and $Pr = 0.005$, respectively. The plateau for all cases corresponds to $K_K \approx 1.6$, consistent with the experimental and numerical value in isotropic turbulence (Sreenivasan 1995; Yeung & Zhou 1997; Ishihara *et al.* 2009).

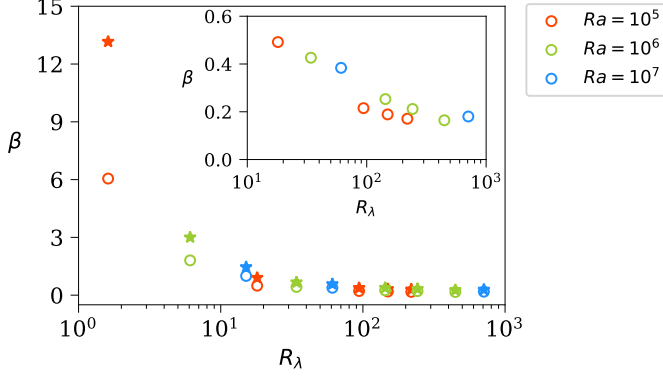


Figure 9: Test of the dissipative anomaly in the bulk of the convection layer using the rescaled mean kinetic energy dissipation rate β , as given by (5.11), versus the Taylor microscale Reynolds number. Asterisks use the integral scale $\mathcal{L} = \ell$ in (5.11), and open circles use $\mathcal{L} = H$. The inset expands the scale for the case $\mathcal{L} = H$. Symbols from left to right in each color correspond to decreasing Pr . The Taylor microscale Reynolds number is given by (5.13).

5.3. Third-order structure function

To further explore whether the velocity fluctuations in the bulk of low- Pr convection are close to Kolmogorov turbulence, we compute the third-order longitudinal structure function defined as

$$S_3(r) = \langle (\delta_L u(r))^3 \rangle, \quad (5.8)$$

where $\langle \cdot \rangle$ denotes an appropriate averaging, and the longitudinal velocity increment is

$$\delta_L u(r) = [\mathbf{u}(\mathbf{x} + \mathbf{r}) - \mathbf{u}(\mathbf{x})] \cdot \hat{\mathbf{r}}, \quad (5.9)$$

with $\hat{\mathbf{r}} = \mathbf{r}/r$. Kolmogorov (1941a) showed that $S_3(r)$ in high- Re homogeneous and isotropic turbulent flow is a universal function of the separation r and varies as

$$S_3(r) = -\frac{4}{5} \varepsilon_u r \quad (5.10)$$

in the inertial range; here and for the remainder of the work $\varepsilon_u := \langle \varepsilon_u \rangle_{A,t}$ ($z = 1/2$). The longitudinal structure functions in the x - and y -directions in midplane for our highest- Re flow show that they are nearly the same for small and moderate increments, so we average in the two directions. We show in figure 8 the averaged third-order structure function in the normalized form $-S_3(r)/(\varepsilon_u r)$ as a function of r/η . The figure shows that the compensated structure function tends to scale with the analytical form of r^2 in the beginning of the viscous range at $r/\eta \sim 1$. It also shows that the normalized structure function exhibits a plateau for an intermediate range of length scales, which implies that $S_3(r)$ indeed approximately varies as r in the inertial range but the numerical value is slightly larger than $4/5$ (Kolmogorov 1941a). One possible reason for this departure is the remnant buoyancy contribution (Yakhot 1992).

5.4. Dissipative anomaly

The zeroth law of turbulence (or “dissipative anomaly”) states that the mean kinetic energy dissipation rate when scaled by a large-scale velocity such as the root-mean-square and the large length scale becomes a constant for sufficiently high Reynolds numbers (Eyink 1994;

Frisch 1995; David & Galtier 2021). Figure 9 displays this rescaled energy dissipation rate

$$\beta = \frac{\varepsilon_u \mathcal{L}}{u_{\text{rms}}^3}, \quad (5.11)$$

where \mathcal{L} is either the height H of the convection layer or the integral scale ℓ calculated from the energy spectrum (5.6) in § 5.2 by

$$\ell = 2\pi \frac{\int_0^\infty k^{-1} E(k) dk}{\int_0^\infty E(k) dk}. \quad (5.12)$$

Note that u_{rms} is also taken with respect to the midplane. The figure summarizes both versions of β versus the Taylor microscale Reynolds number

$$R_\lambda = \left(\frac{25Ra}{9\varepsilon_u^2 Pr} \right)^{1/4} u_{\text{rms}}^2 \quad (5.13)$$

in the bulk region of the flow. The data for different Rayleigh and Prandtl numbers collapse nicely on a curve that saturates at an approximate value of 0.2 (see the inset of the figure). While this is smaller than 0.45 found by Sreenivasan (1998) for isotropic turbulence, the result implies that the strongly disparate viscous and thermal boundary layer widths (and thus the plume stem widths) do not matter for the driving of the turbulence cascade in the bulk of the flow. However, it also highlights the intrinsic difference in dissipation between convection and isotropic turbulence.

6. Characteristic lengths and times of turbulent superstructures

The characteristic length scale of the dominant energy-containing structures is of the order of the size of the system when $\Gamma \approx 1$, e.g., a large-scale circulation covering the entire domain (Schumacher *et al.* 2016; Zürner *et al.* 2019; Zwirner *et al.* 2020). However, for $\Gamma \gg 1$, mean circulation rolls with diameters larger than H are observed (Emran & Schumacher 2015); the resulting large-scale patterns of these rolls are termed turbulent superstructures of convection (Pandey *et al.* 2018; Stevens *et al.* 2018; Fonda *et al.* 2019; Green *et al.* 2020) as we stated already in § 1. Although the superstructures extend all the way from the bottom to the top plate (Pandey *et al.* 2018), they are conspicuous when the vertical velocity u_z , temperature T , or the vertical heat flux $u_z T$ fields are visualized in the midplane (Fonda *et al.* 2019; Green *et al.* 2020). For instance, figure 1 shows turbulent superstructures for low- Pr convection in the form of hot upflows and cold downflows.

The characteristic length λ of the superstructures is the typical distance between two consecutive upwelling or downwelling regions and can be estimated using one-dimensional (1D) spectra of the thermal variance, kinetic energy, and convective heat flux in a horizontal plane (Hartlep *et al.* 2003; Pandey *et al.* 2018; Stevens *et al.* 2018; Green *et al.* 2020; Krug *et al.* 2020). It can also be estimated by computing the two-point auto-correlation function of u_z or T in a horizontal plane and identifying the location of the first minimum, corresponding to $\lambda/2$ (Pandey *et al.* 2018).

We compute the 1D power spectra of the vertical velocity, temperature, and convective

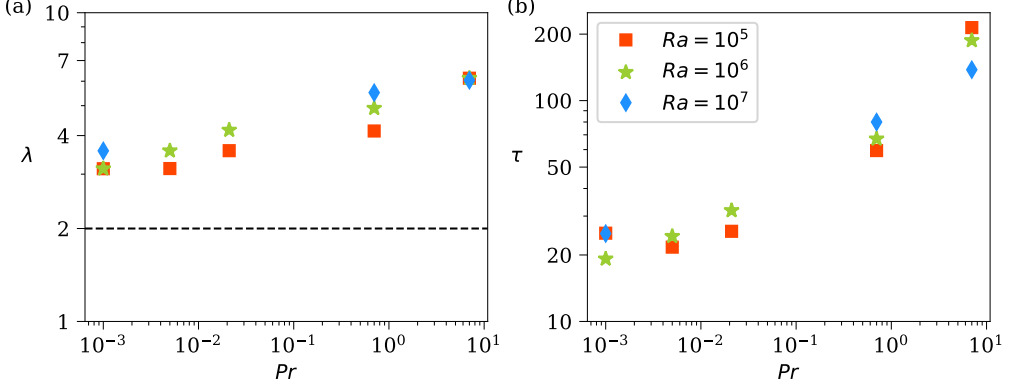


Figure 10: Characteristic spatial (a) and temporal (b) scales of the turbulent superstructures as a function of Pr . Both temporal and spatial scales decrease with decreasing Prandtl number, but seem to level off for $Pr \leq 0.005$.

heat flux, all averaged with respect to the azimuthal angle. They are given by

$$S_U(k) = \frac{1}{2\pi} \int_0^{2\pi} |\hat{U}_z(k, \phi_k)|^2 d\phi_k, \quad (6.1)$$

$$S_\Theta(k) = \frac{1}{2\pi} \int_0^{2\pi} |\hat{\Theta}(k, \phi_k)|^2 d\phi_k, \quad (6.2)$$

$$S_{U\Theta}(k) = \frac{1}{2\pi} \int_0^{2\pi} \Re[\hat{U}_z^*(k, \phi_k) \hat{\Theta}(k, \phi_k)] d\phi_k, \quad (6.3)$$

where $\hat{U}_z(k, \phi_k)$ and $\hat{\Theta}(k, \phi_k)$ are, respectively, the 2D Fourier transforms of $u_z(x, y, H/2)$ and $\theta(x, y, H/2)$. Note that the spectrum $S_U(k)$ differs from the energy spectrum $E(k)$ defined in § 5.2. We find that the three spectra exhibit a peak at nearly the same wavenumber k_{\max}^ω corresponding to the maximum of $S_\omega(k)$ (see figure 13), yielding the characteristic spatial scale $\lambda_\omega = 2\pi/k_{\max}^\omega$ of the superstructures, with $\omega = \{U, \Theta, U\Theta\}$.

Pandey *et al.* (2018, 2021) found that the characteristic scales λ_U and λ_Θ do not always agree with each other, the contrast being usually larger at moderate and high Prandtl numbers. Here, we extract the spatial scale of superstructures from the power spectrum of the convective heat flux (see also Hartlep *et al.* (2003) and Krug *et al.* (2020)). It was observed in Pandey *et al.* (2018) that λ is a function of Pr and the maximum of $\lambda(Pr)$ was found at $Pr \approx 7$ for $Ra = 10^5$. In the present simulations (in which the Pr range has been extended down to 0.001 and Ra by two orders of magnitude), the corresponding values of λ as a function of Pr are plotted in figure 10(a) for all simulations of table 1. We find that λ decreases with decreasing Pr but they seem to level off at $\lambda \approx 3H$ for the lowest Prandtl numbers of 0.005 and 0.001; see also figure 11 where the magnitude of λ is displayed in the streamline plot. It remains to be studied as to how this scale arises starting from the onset of RBC where $\lambda = 2.02H$ independently of Pr (Chandrasekhar 1981), as indicated in figure 10(a) as a dashed horizontal line. We also refer to Appendix C for further details.

The characteristic temporal scale (τ) of the superstructures is long compared to the time scale of the turbulent fluctuations. Thus, time-averaging the velocity or temperature fields over a time interval τ yields coarse-grained fields, which are nearly devoid of the small-scale fluctuations. The coarse-grained large-scale structures evolve on the time scales which are of

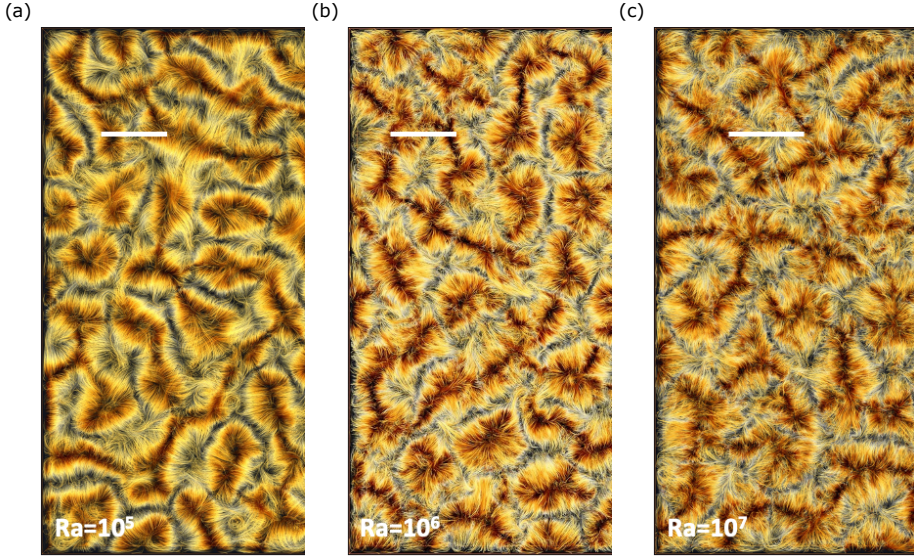


Figure 11: Plots of streamlines for snapshots at (a) $Ra = 10^5$, (b) 10^6 , and (c) 10^7 , all at $Pr = 0.001$. The view is from the top. Only one half of the cross-section is shown. The corresponding values of λ are indicated by a horizontal white bar in each panel.

the order of τ (Pandey *et al.* 2018; Fonda *et al.* 2019), related to the time for a fluid parcel to complete a circulation. It is computed as

$$\tau = 3 \frac{\pi(\lambda/4 + H/2)}{u_{\text{rms}}}, \quad (6.4)$$

where the quantity in the numerator is the circumference of superstructure rolls with elliptical cross-section (Pandey *et al.* 2018). The factor of three in the above expression arises from the fact that the circulation time in an extended convection flow is not fixed but exhibits a broad distribution with stretched-exponential tails in the Lagrangian frame of reference along massless tracer trajectories (Schneide *et al.* 2018; Vieweg *et al.* 2021b). The scale computed using expression (6.4) is plotted in figure 10(b) as a function of Pr . We find that τ increases with Pr , consistent with the fact that the Reynolds number, and thus the characteristic velocity u_{rms} , decreases with increasing Pr , requiring a longer time for fluid parcels to complete a circulation. Note that λ in equation (6.4) also increases with increasing Pr , but the increase is not as significant as the decrease in u_{rms} .

7. Conclusions and outlook

Our focus here has been the Rayleigh-Bénard convection in a horizontally extended layer for molecular Prandtl numbers as small as $Pr = 10^{-3}$, which go beyond those accessible in controlled laboratory experiments and approach astrophysical conditions. We extended the parameter space of previous works by Pandey *et al.* (2018) and Fonda *et al.* (2019) by direct numerical simulations, both towards lower Pr and higher Ra , and thus determined more conclusively various parameter dependencies such as global heat and momentum transports, temperature fluctuations, as well as the kinetic and thermal dissipation rates. Among others, these results provide a test for existing predictions by the theory of Grossmann & Lohse (2001) and Stevens *et al.* (2013). Comparisons show that the predictions for the global heat

and momentum transports as a function of the Prandtl number at fixed Rayleigh number are in fair agreement.

We also found that the Nusselt number decreases as $Nu \sim Pr^{0.19}$, whereas the Reynolds number increases approximately as $Re \sim Pr^{-0.6}$ when the Prandtl number decreases from $Pr = 0.7$ to 0.001 as detailed in table 2. The dimensionless mean thermal and kinetic energy dissipation rates also decrease with increasing Pr and their scaling behaviors are consistent with that of the global heat transport. We studied the depth dependence of these quantities, and found that, due to a high diffusive temperature field in convection at very low Pr , the bulk fluid is not mixed well and a significant vertical temperature gradient occurs in the bulk region, even for the highest accessible Rayleigh number.

The highly inertial fluid turbulence in the bulk of low- Pr convection layer was studied by examining the kinetic energy spectra, the 4/5-ths law, local isotropy, and a test of the dissipative anomaly. The results suggest that the fluid turbulence in the bulk for the lowest Prandtl number is close to the classical Kolmogorov turbulence. This implies that the temperature field behaves as a passive and highly diffusive scalar stirred by a highly turbulent flow; the impact of thermal plumes, which are the unstable fragments of the thick thermal boundary layers, can be considered an efficient large-scale forcing for turbulence, dominantly in the lower wavenumber part of the inertial range (k_T in figure 7). Some differences do remain. In particular, the asymptotic value of the rescaled mean kinetic energy dissipation rate falls below that in isotropic turbulence (Sreenivasan 1998), which suggests that boundary layers do matter, despite the nearness to isotropy in the central region.

Our DNS results are fully resolved and can thus have implications for the modeling of small-scale turbulence in coarser-grid simulation studies of mesoscale convection, particularly for the development of subgrid-scale models that go beyond the mixing length theory of Prandtl (1925). This class of algebraic turbulence models is still a workhorse in astrophysical simulations; see for example discussions of their limitations and extensions in Miesch (2005) and Kupka & Muthsam (2017), or recent extensions by Brandenburg (2016). Finally, we stress that the convection considered here does not incorporate complexities such as rotation, magnetic field, varying molecular transport coefficients, or curvature, which are present in geophysical and astrophysical settings. They would have to be included to yield realistic models in these specific instances. The present focus has been the exploration of the effects of low Prandtl numbers, which is an important facet of these flows. A more detailed study of these points in connection with small-scale intermittency in low-Prandtl-number RBC flows is underway, and will be reported elsewhere.

Acknowledgements. The authors gratefully acknowledge the Gauss Centre for Supercomputing e.V. (<https://www.gauss-centre.eu>) for funding this project by providing computing time on the GCS Supercomputer SuperMUC-NG at Leibniz Supercomputing Centre (<https://www.lrz.de>).

Funding. A.P. acknowledges support from the Deutsche Forschungsgemeinschaft (DFG) within the Priority Programme “Turbulent Superstructures” under Grant No. DFG-SPP 1881. This work was also supported by Grant No. SCHU 1410/30-1 of DFG and NYUAD Institute Grant G1502 “NYUAD Center for Space Science.” D.K. is partly supported by Grant No. KR 4445/2-1 of DFG.

Declaration of Interests. The authors report no conflict of interest.

Data availability statement. The data that support the findings of this study are available from the corresponding author upon reasonable request.

Author ORCIDs.

A. Pandey, <https://orcid.org/0000-0001-8232-6626>;
D. Krasnov, <https://orcid.org/0000-0002-8339-7749>;
K.R. Sreenivasan, <https://orcid.org/0000-0002-3943-6827>;
J. Schumacher, <https://orcid.org/0000-0002-1359-4536>

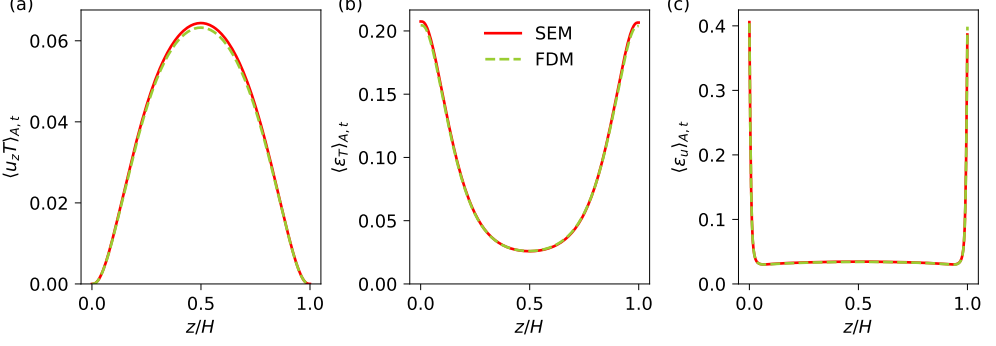


Figure 12: Vertical profiles of (a) the convective heat flux, (b) the thermal dissipation rate, and (c) the kinetic energy dissipation rate computed using the spectral element (solid red curves) and the finite difference (dashed green curves) solvers for $Pr = 0.005$, $Ra = 10^5$ agree very well each other.

Appendix A. Comparison of the spectral element and finite difference solvers

As mentioned in § 2, we use two different solvers, one based on the spectral element method (SEM) and one based on the finite difference method (FDM), to perform our simulations due to the demanding requirements at very low Prandtl numbers. Therefore, it is important to ensure that both the solvers yield the same results. To check this, we performed comparison simulations, for $Pr = 0.005$ and $Ra = 10^5$ and for $Pr = 0.7$ and $Ra = 10^7$. In figure 12, we plot the vertical profiles of the convective heat flux, the thermal, and the kinetic energy dissipation rates for the former comparison. The profiles from both the spectral element and finite difference solvers agree very well with each other. The globally-averaged quantities such as the Nusselt and the Reynolds numbers also agree excellently.

The global heat flux can also be estimated using the global dissipation rates from the exact relations (Howard 1972), and their concurrence is also an indicator of the sufficiency of the spatial and temporal resolutions (Pandey *et al.* 2021). The exact relations yield the Nusselt numbers as

$$Nu_{\varepsilon_u} = 1 + \sqrt{RaPr} \langle \varepsilon_u \rangle_{V,t}, \quad (\text{A } 1)$$

$$Nu_{\varepsilon_T} = \sqrt{RaPr} \langle \varepsilon_T \rangle_{V,t}. \quad (\text{A } 2)$$

Further, the heat flux $Nu(z)$ in each horizontal plane, see (4.3) in the main text, remains a constant across the convection layer in the statistically steady state and matches with Nu . We thus compute the averaged heat flux at the top and bottom plates as

$$Nu_{\partial_z T} = - \left\langle \left(\frac{\partial T}{\partial z} \right)_{z=0,H} \right\rangle_{A,t} \quad (\text{A } 3)$$

and list it along with Nu , Nu_{ε_u} , Nu_{ε_T} in table 4. The results in the table show that the agreement between all differently obtained Nusselt numbers is excellent for all the simulations.

A few words on the determination of the kinetic energy dissipation rate from the results of the FDM solver. It has been shown in Viré & Knaepen (2009) that, for the rate of strain tensor $S_{ij} = (\partial u_i / \partial x_j + \partial u_j / \partial x_i) / 2$, the identity $S_{ij} S_{ij} = -u_i \partial S_{ij} / \partial x_j + \partial(u_i S_{ij}) / \partial x_j$ is not fulfilled in discrete form, which is particularly relevant to finite-difference and finite-volume methods. The direct computation of $S_{ij} S_{ij}$ tends to yield underpredicted values, especially if the discretization errors are large. For example, in case of coarse grids, more pertinent to

Pr	Ra	No. of mesh cells	Nu	Nu_{ε_u}	Nu_{ε_T}	$Nu_{\partial_z T}$	$t_{\text{sim}}(t_f)$
0.001	10^5	$9600 \times 9600 \times 640$	1.21 ± 0.003	1.22 ± 0.001	1.22 ± 0.003	1.22 ± 0.003	5.4
0.005	10^5	2367488×11^3	1.86 ± 0.02	1.85 ± 0.02	1.86 ± 0.02	1.86 ± 0.02	60
0.005	10^5	$8192 \times 8192 \times 512$	1.84 ± 0.001	1.84 ± 0.002	1.84 ± 0.001	1.84 ± 0.001	3.5
0.021	10^5	2367488×7^3	2.62 ± 0.02	2.62 ± 0.02	2.62 ± 0.02	2.62 ± 0.02	156
0.7	10^5	1352000×5^3	4.26 ± 0.03	4.26 ± 0.03	4.26 ± 0.03	4.26 ± 0.02	1108
7	10^5	1352000×5^3	4.14 ± 0.02	4.14 ± 0.02	4.14 ± 0.02	4.14 ± 0.01	2670
0.001	10^6	$12800 \times 12800 \times 800$	2.48 ± 0.003	2.47 ± 0.02	2.48 ± 0.01	2.48 ± 0.01	2.0
0.005	10^6	$8192 \times 8192 \times 512$	3.52 ± 0.02	3.51 ± 0.03	3.52 ± 0.02	3.52 ± 0.02	6.3
0.021	10^6	$8192 \times 8192 \times 512$	4.84 ± 0.01	4.81 ± 0.02	4.81 ± 0.03	4.81 ± 0.02	6.0
0.7	10^6	2367488×7^3	8.10 ± 0.06	8.10 ± 0.04	8.10 ± 0.04	8.10 ± 0.03	1292
7	10^6	2367488×7^3	8.30 ± 0.05	8.30 ± 0.04	8.30 ± 0.02	8.30 ± 0.02	3255
0.001	10^7	$20480 \times 20480 \times 1280$	4.57 ± 0.01	4.56 ± 0.10	4.59 ± 0.01	4.59 ± 0.01	1.0
0.7	10^7	2367488×11^3	15.48 ± 0.13	15.48 ± 0.08	15.48 ± 0.06	15.48 ± 0.10	248
0.7	10^7	$6720 \times 6720 \times 420$	15.50 ± 0.10	15.57 ± 0.03	15.52 ± 0.03	15.52 ± 0.03	10
7	10^7	1352000×11^3	16.25 ± 0.08	16.25 ± 0.05	16.25 ± 0.03	16.25 ± 0.02	471

Table 4: The turbulent heat flux, which is computed in four different ways, agrees very well for all reported simulations. The error bars indicate the standard deviation. t_{sim} is the total simulation time in the statistically steady state. The time advancement by one free-fall time unit for the biggest simulation took 30 million core hours on 144000 processor cores on the cluster SuperMUC-NG at Leibniz Rechenzentrum Garching.

LES however, the difference between direct computation of $S_{ij}S_{ij}$ and summation-by-parts can yield a factor of 2 to 2.5 in the buffer and logarithmic layer regions (Viré *et al.* 2011). Albeit this difference scales as $\sim O(h^2)$ (with h being the mesh step-size) for the 2nd-order approximations, it cannot be completely neglected, even in case of finer resolutions used in DNS. Here, we cannot directly apply the summation-by-parts approach, since it involves the so-called flux-variables, prescribed at the cell interface (Viré *et al.* 2011). These flux-variables are used in the algorithm to secure divergence-free condition and conservative form of the non-linear terms, but not stored. We have applied a different approach for the FDM results – the S_{ij} tensor is computed by using 6th-order accurate stencils for the velocity gradients to reduce the effect of discretization errors.

Appendix B. Grid sensitivity for our biggest simulation

The Kolmogorov length scale in the flow for $Pr = 0.001$ and $Ra = 10^7$ becomes very small and, consequently, computational resources required for the numerical investigation of this flow become exorbitant. Therefore, to determine the optimum number of nodes needed to resolve the flow adequately, we performed this simulation on three different grids with $15360 \times 15360 \times 1024$, $20480 \times 20480 \times 1280$, and $22400 \times 22400 \times 1400$ mesh cells, which we denote in the following as mesh-1, mesh-2, and mesh-3, respectively. As summarized in Scheel *et al.* (2013), we compare the horizontally as well as the globally averaged quantities from these simulations to test the effects of grid resolution. The kinetic energy dissipation rate field $\varepsilon_u(\mathbf{x}, t)$, which involves the computation of all the nine terms of the velocity gradient tensor, is very sensitive to the mesh size in a low- Pr convection. We computed the horizontally-averaged kinetic energy dissipation rate $\langle \varepsilon_u \rangle_{A,t}(z)$ and investigated the region near the midplane where the computational grid is coarsest. We observed underresolved data for mesh-1, whereas the variation of $\langle \varepsilon_u \rangle_{A,t}(z)$ is smooth for simulations with mesh-2 and mesh-3. Furthermore, $\langle \varepsilon_u \rangle_{A,t}(z)$ from mesh-2 and mesh-3 agree very well, in particular

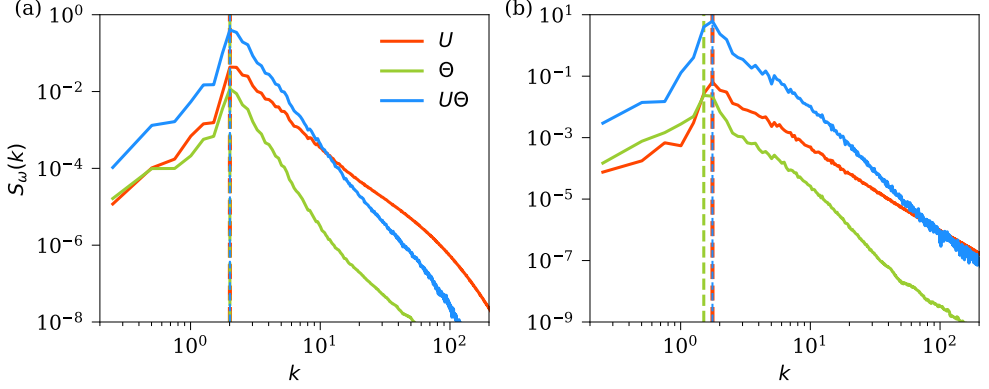


Figure 13: Power spectra S_U , S_Θ , and $S_{U\Theta}$ as defined in equations (6.1)–(6.3) in the midplane for $Pr = 0.001$ at (a) $Ra = 10^5$ and (b) $Ra = 10^7$. They exhibit peak at nearly the same wavenumber corresponding to the characteristic spatial scale (or wavelength) of the turbulent superstructures of convection.

they both yield the same relative difference between the results of 2nd- and 6th-order stencils applied for the direct computation of the velocity gradients. This analysis clearly indicates that mesh-2 is able to properly capture the velocity derivatives for these extreme parameters. Thus, we carried out our simulation for $Pr = 0.001$ and $Ra = 10^7$ with mesh-2.

Appendix C. Estimation of the characteristic lengths and times of superstructures

We show the power spectra $S_U(k)$, $S_\Theta(k)$, and $S_{U\Theta}(k)$ for $Pr = 0.001$ at $Ra = 10^5$ and $Ra = 10^7$ in figure 13 and find that the spectral distributions for the velocity and temperature fields are different. Figure 13 shows that the power first increases with decreasing length scales and attains a maximum before declining sharply with further decrease in the scale size. We find that the decay of the thermal variance spectrum beyond k_{\max} is rapid compared to that of the squared vertical velocity component. This is because the velocity field in very-low- Pr convection is vigorously turbulent and possesses larger fine-scale contributions compared to the predominantly large-scale nature of the temperature field (Schumacher *et al.* 2015). We find, however, that the three spectra exhibit a peak at nearly the same wavenumber k_{\max}^ω corresponding to the maximum of $S_\omega(k)$, yielding the characteristic spatial scale $\lambda_\omega = 2\pi/k_{\max}^\omega$ of the superstructures, with $\omega = \{U, \Theta, U\Theta\}$.

Furthermore, the spatial scale does not remain fixed but fluctuates during the evolution of the flow. This can be seen in figure 14, where we plot $k_{\max}^{U\Theta}(t)$, extracted from each instantaneous snapshot of our simulations, as a function of time. The figure shows that $k_{\max}^{U\Theta}$ is independent of time for the entire duration of simulations for $Pr = 0.001$. The same comment also holds for $Pr = 0.005$ and $Pr = 0.021$ simulations (not shown in the figure). However, $k_{\max}^{U\Theta}$ for the simulations at $Pr = 0.7$ and $Pr = 7$, though remaining fixed for most of the time, shows occasional excursions. Thus, we determine the characteristic spatial scale of superstructures by time averaging $k_{\max}^{U\Theta}(t)$ and finding $\lambda = 2\pi/\langle k_{\max}^{U\Theta}(t) \rangle_t$.

REFERENCES

- AHLERS, G., GROSSMANN, S. & LOHSE, D. 2009 Heat transfer and large scale dynamics in turbulent Rayleigh-Bénard convection. *Rev. Mod. Phys.* **81**, 503–537.
 AURNOU, J., CALKINS, M., CHENG, J., JULIEN, K., KING, E., NIEVES, D., SODERLUND, K. & STELLMACH, S.

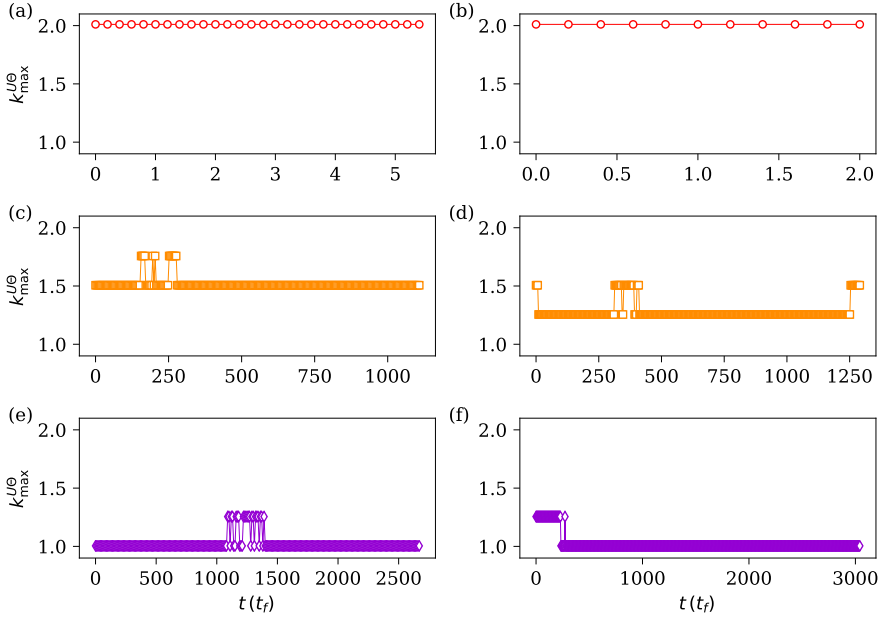


Figure 14: Temporal evolution of the peak wavenumber k_{\max} for $Ra = 10^5$ (a,c,e) and $Ra = 10^6$ (b,d,f). The location of maximum does not change for $Pr = 0.001$ (a,b), whereas it occasionally shifts towards the higher wavenumber for $Pr = 0.7$ (c,d) and also for $Pr = 7$ (e,f).

- 2015 Rotating convective turbulence in Earth and planetary cores. *Phys. Earth Planet. Inter.* **246**, 52–71.
- BAILON-CUBA, J., EMRAN, M. S. & SCHUMACHER, J. 2010 Aspect ratio dependence of heat transfer and large-scale flow in turbulent convection. *J. Fluid Mech.* **655**, 152–173.
- BHATTACHARYA, S., VERMA, M. K. & SAMTANEY, R. 2021 Prandtl number dependence of the small-scale properties in turbulent Rayleigh–Bénard convection. *Phys. Rev. Fluids* **6**, 063501.
- BOLGIANO, R. 1959 Turbulent spectra in a stably stratified atmosphere. *J. Geophys. Res.* **64**, 2226.
- BRANDENBURG, A. 2016 Stellar mixing length theory with entropy rain. *Astrophys. J.* **832** (1), 6.
- BRANDENBURG, A. & SUBRAMANIAN, K. 2005 Astrophysical magnetic fields and nonlinear dynamo theory. *Phys. Rep.* **417**, 1–209.
- BREUER, M., WESSLING, S., SCHMALZL, J. & HANSEN, U. 2004 Effect of inertia in Rayleigh–Bénard convection. *Phys. Rev. E* **69**, 026302.
- CALKINS, M. A., AURNOU, J. M., ELDERIDGE, J. D. & JULIEN, K. 2012 The influence of fluid properties on the morphology of core turbulence and the geomagnetic field. *Earth Planet. Sci. Lett.* **359**, 55–60.
- CATTANEO, F., LENZ, D. & WEISS, N. 2001 On the origin of the solar mesogranulation. *Astrophys. J.* **563** (1), L91–L94.
- CHANDRASEKHAR, S. 1981 *Hydrodynamic and Hydromagnetic Stability*. New York: Dover.
- CHILLÀ, F. & SCHUMACHER, J. 2012 New perspectives in turbulent Rayleigh–Bénard convection. *Eur. Phys. J. E* **35**, 58.
- CIONI, S., CILIBERTO, S. & SOMMERIA, J. 1997 Strongly turbulent Rayleigh–Bénard convection in mercury: comparison with results at moderate Prandtl number. *J. Fluid Mech.* **335**, 111–140.
- DAVID, V. & GALTIER, S. 2021 Proof of the zeroth law of turbulence in one-dimensional compressible magnetohydrodynamics and shock heating. *Phys. Rev. E* **103**, 063217.
- EMRAN, M. S. & SCHUMACHER, J. 2008 Fine-scale statistics of temperature and its derivatives in convective turbulence. *J. Fluid Mech.* **611**, 13.
- EMRAN, M. S. & SCHUMACHER, J. 2015 Large-scale mean patterns in turbulent convection. *J. Fluid Mech.* **776**, 96–108.

- EYINK, G. L. 1994 Energy dissipation without viscosity in ideal hydrodynamics I. Fourier analysis and local energy transfer. *Physica D: Nonlinear Phenomena* **78** (3), 222–240.
- FISCHER, P. F. 1997 An overlapping Schwarz method for spectral element solution of the incompressible Navier-Stokes equations. *J. Comp. Phys.* **133** (1), 84–101.
- FONDA, E., PANDEY, A., SCHUMACHER, J. & SREENIVASAN, K. R. 2019 Deep learning in turbulent convection networks. *Proc. Natl. Acad. Sci. USA* **116** (18), 8667–8672.
- FRISCH, U. 1995 *Turbulence: The Legacy of A. N. Kolmogorov*. Cambridge: Cambridge University Press.
- GARAUD, P. 2021 Journey to the center of stars: The realm of low Prandtl number fluid dynamics. *Phys. Rev. Fluids* **6**, 030501.
- GREEN, G., VLAYKOV, D. G., MELLADO, J. P. & WILCZEK, M. 2020 Resolved energy budget of superstructures in Rayleigh–Bénard convection. *J. Fluid Mech.* **887**, A21.
- GROSSMANN, S. & LOHSE, D. 2000 Scaling in thermal convection: a unifying theory. *J. Fluid Mech.* **407**, 27–56.
- GROSSMANN, S. & LOHSE, D. 2001 Thermal convection for large Prandtl numbers. *Phys. Rev. Lett.* **86**, 3316.
- GUERVILLY, C., CARDIN, P. & SCHAEFFER, N. 2019 Turbulent convective length scale in planetary cores. *Nature* **570**, 368–371.
- HARTLER, T., TILGNER, A. & BUSSE, F. H. 2003 Large scale structures in Rayleigh–Bénard convection at high Rayleigh numbers. *Phys. Rev. Lett.* **91**, 064501.
- HARTLER, T., TILGNER, A. & BUSSE, F. H. 2005 Transition to turbulent convection in a fluid layer heated from below at moderate aspect ratio. *J. Fluid Mech.* **544**, 309–322.
- HORANYI, S., KREBS, L. & MÜLLER, U. 1999 Turbulent Rayleigh–Bénard convection in low Prandtl-number fluids. *Int. J. Heat Mass Transfer* **42** (21), 3983–4003.
- HOWARD, L. N. 1972 Bounds on flow quantities. *Annu. Rev. Fluid Mech.* **4** (1), 473–494, arXiv: <https://doi.org/10.1146/annurev.fl.04.010172.002353>.
- ISHIHARA, T., GOTOH, T. & KANEDA, Y. 2009 Study of high-Reynolds number isotropic turbulence by direct numerical simulation. *Annu. Rev. Fluid Mech.* **41**, 165–180.
- KADANOFF, L. P. 2001 Turbulent heat flow: Structures and scaling. *Phys. Today* **54**, 34–39.
- KÄPYLÄ, P. J. 2021 Prandtl number dependence of stellar convection: Flow statistics and convective energy transport. *A&A* **655**, A78.
- KOLMOGOROV, A. N. 1941a Dissipation of energy in locally isotropic turbulence. *Dokl. Akad. Nauk SSSR* **32**, 16–18.
- KOLMOGOROV, A. N. 1941b The local structure of turbulence in incompressible viscous fluid for very large Reynolds numbers. *Dokl. Akad. Nauk SSSR* **30**, 301–305.
- KRASNOV, D., ZIKANOV, O. & BOECK, T. 2011 Comparative study of finite difference approaches in simulation of magnetohydrodynamic turbulence at low magnetic Reynolds number. *Comput. Fluids* **50** (1), 46–59.
- KRUG, D., LOHSE, D. & STEVENS, R. J. A. M. 2020 Coherence of temperature and velocity superstructures in turbulent Rayleigh–Bénard flow. *J. Fluid Mech.* **887**, A2.
- KUPKA, F. & MUTHSAM, H. J. 2017 Modelling of stellar convection. *Living Rev. Comput. Astrophys.* **3**, 1.
- LENZI, S., VON HARDENBERG, J. & PROVENZALE, A. 2021 Scale of plume clustering in large-Prandtl-number convection. *Phys. Rev. E* **103**, 053103.
- LIU, W., KRASNOV, D. & SCHUMACHER, J. 2018 Wall modes in magnetoconvection at high Hartmann numbers. *J. Fluid Mech.* **849**, R2.
- LOHSE, D. & XIA, K.-Q. 2010 Small-scale properties of turbulent Rayleigh–Bénard convection. *Annu. Rev. Fluid Mech.* **42**, 335–364.
- MIESCH, M. S. 2005 Large-scale dynamics of the convective zone and tachocline. *Living Rev. Solar Phys.* **2**, 1.
- MISHRA, P. K. & VERMA, M. K. 2010 Energy spectra and fluxes for Rayleigh–Bénard convection. *Phys. Rev. E* **81**, 056316.
- MOLLER, S., KÄUFER, T., PANDEY, A., SCHUMACHER, J. & CIERPKA, C. 2022 Combined particle image velocimetry and thermometry of turbulent superstructures in thermal convection. *J. Fluid Mech.*, *in press*.
- MONIN, A. S. & YAGLOM, A. M. 2007 *Statistical Fluid Mechanics*. Mineola, NY: Dover Publications Inc.
- NATH, D., PANDEY, A., KUMAR, A. & VERMA, M. K. 2016 Near isotropic behavior of turbulent thermal convection. *Phys. Rev. Fluids* **1**, 064302.
- NORDLUND, A., STEIN, R. & ASPLUND, M. 2009 Solar surface convection. *Living Rev. Sol. Phys.* **6**, 2.

- PANDEY, A. 2021 Thermal boundary layer structure in low-Prandtl-number turbulent convection. *J. Fluid Mech.* **910**, A13.
- PANDEY, A., SCHEEL, J. D. & SCHUMACHER, J. 2018 Turbulent superstructures in Rayleigh-Bénard convection. *Nat. Commun.* **9**, 2118.
- PANDEY, A., SCHUMACHER, J. & SREENIVASAN, K. R. 2021 Non-Boussinesq low-Prandtl-number convection with a temperature-dependent thermal diffusivity. *Astrophys. J.* **907** (1), 56.
- PANDEY, A. & SREENIVASAN, K. R. 2021 Convective heat transport in slender cells is close to that in wider cells at high Rayleigh and Prandtl numbers. *Europhys. Lett.* **135** (2), 24001.
- PANDEY, A. & VERMA, M. K. 2016 Scaling of large-scale quantities in Rayleigh-Bénard convection. *Phys. Fluids* **28** (9), 095105.
- PELTIER, L. J., WYNGAARD, J. C., KHANNA, S. & BRASSEUR, J. O. 1996 Spectra in the unstable surface layer. *J. Atmos. Sci.* **53** (1), 49–61.
- PRANDTL, L. 1925 Bericht über Untersuchungen zur ausgebildeten Turbulenz. *Z. Angew. Math. Mech.* **5**, 136–139.
- RINCON, F., LIGNIÈRES, F. & RIEUTORD, M. 2005 Mesoscale flows in large aspect ratio simulations of turbulent compressible convection. *A&A* **430** (3), L57–L60.
- RINCON, F. & RIEUTORD, M. 2018 The Sun's supergranulation. *Living Rev. Sol. Phys.* **15**, 6.
- SCHEEL, J. D., EMRAN, M. S. & SCHUMACHER, J. 2013 Resolving the fine-scale structure in turbulent Rayleigh-Bénard convection. *New J. Phys.* **15**, 113063.
- SCHEEL, J. D., KIM, E. & WHITE, K. R. 2012 Thermal and viscous boundary layers in turbulent Rayleigh-Bénard convection. *J. Fluid Mech.* **711**, 281–305.
- SCHEEL, J. D. & SCHUMACHER, J. 2014 Local boundary layer scales in turbulent Rayleigh-Bénard convection. *J. Fluid Mech.* **758**, 344–373.
- SCHEEL, J. D. & SCHUMACHER, J. 2016 Global and local statistics in turbulent convection at low Prandtl numbers. *J. Fluid Mech.* **802**, 147–173.
- SCHEEL, J. D. & SCHUMACHER, J. 2017 Predicting transition ranges to fully turbulent viscous boundary layers in low Prandtl number convection flows. *Phys. Rev. Fluids* **2**, 123501.
- SCHINDLER, F., ECKERT, S., ZÜRNER, T., SCHUMACHER, J. & VOGT, T. 2022 Collapse of coherent large scale flow in strongly turbulent liquid metal convection. *Phys. Rev. Lett.* **128**, 164501.
- SCHMALZL, J., BREUER, M. & HANSEN, U. 2004 On the validity of two-dimensional numerical approaches to time-dependent thermal convection. *Europhys. Lett.* **67**, 390–396.
- SCHNEIDE, C., PANDEY, A., PADBERG-GEHLE, K. & SCHUMACHER, J. 2018 Probing turbulent superstructures in Rayleigh-Bénard convection by Lagrangian trajectory clusters. *Phys. Rev. Fluids* **3**, 113501.
- SCHUMACHER, J., BANDARU, V., PANDEY, A. & SCHEEL, J. D. 2016 Transitional boundary layers in low-Prandtl-number convection. *Phys. Rev. Fluids* **1**, 084402.
- SCHUMACHER, J., GÖTZFRIED, P. & SCHEEL, J. D. 2015 Enhanced enstrophy generation for turbulent convection in low-Prandtl-number fluids. *Proc. Natl. Acad. Sci. USA* **112**, 9530–9535.
- SCHUMACHER, J. & SREENIVASAN, K. R. 2020 Colloquium: Unusual dynamics of convection in the Sun. *Rev. Mod. Phys.* **92**, 041001.
- SHRAIMAN, B. I. & SIGGIA, E. D. 1990 Heat transport in high-Rayleigh-number convection. *Phys. Rev. A* **42**, 3650–3653.
- SIGGIA, E. D. 1994 High Rayleigh number convection. *Annu. Rev. Fluid Mech.* **26**, 137.
- SREENIVASAN, K. R. 1984 On the scaling of the turbulence energy dissipation rate. *Phys. Fluids* **27**, 1048–1051.
- SREENIVASAN, K. R. 1995 On the universality of the Kolmogorov constant. *Phys. Fluids* **7** (11), 2778–2784.
- SREENIVASAN, K. R. 1998 An update on the energy dissipation rate in isotropic turbulence. *Phys. Fluids* **10** (2), 528–529.
- SREENIVASAN, K. R. & SCHUMACHER, J. 2010 Lagrangian views on turbulent mixing of passive scalars. *Phil. Trans. R. Soc. A* **368**, 1561–1577.
- STEVENS, R., LOHSE, D. & VERZICCO, R. 2011 Prandtl and Rayleigh number dependence of heat transport in high Rayleigh number thermal convection. *J. Fluid Mech.* **688**, 31–43.
- STEVENS, R. J. A. M., BLASS, A., ZHU, X., VERZICCO, R. & LOHSE, D. 2018 Turbulent thermal superstructures in Rayleigh-Bénard convection. *Phys. Rev. Fluids* **3**, 041501.
- STEVENS, R. J. A. M., VAN DER POEL, E. P., GROSSMANN, S. & LOHSE, D. 2013 The unifying theory of scaling in thermal convection: the updated prefactors. *J. Fluid Mech.* **730**, 295–308.
- TRITTON, D. J. 1977 *Physical Fluid Dynamics*. Dordrecht: Springer Netherlands.

- VAN DER POEL, E. P., STEVENS, R. J. A. M. & LOHSE, D. 2013 Comparison between two- and three-dimensional Rayleigh-Bénard convection. *J. Fluid Mech.* **736**, 177–194.
- VERMA, M. K. 2018 *Physics of Buoyant Flows*. Singapore: World Scientific.
- VERMA, M. K., KUMAR, A. & PANDEY, A. 2017 Phenomenology of buoyancy-driven turbulence: recent results. *New J. Phys.* **19** (2), 025012.
- VERZICCO, R. & CAMUSSI, R. 1999 Prandtl number effects in convective turbulence. *J. Fluid Mech.* **383**, 55–73.
- VIEWEG, P. P., SCHEEL, J. D. & SCHUMACHER, J. 2021a Supergranule aggregation for constant heat flux-driven turbulent convection. *Phys. Rev. Research* **3**, 013231.
- VIEWEG, P. P., SCHNEIDE, C., PADBERG-GEHLE, K. & SCHUMACHER, J. 2021b Lagrangian heat transport in turbulent three-dimensional convection. *Phys. Rev. Fluids* **6**, L041501.
- VIRÉ, A. & KNAEPEN, B. 2009 On discretization errors and subgrid scale model implementations in Large Eddy Simulations. *J. Comp. Phys.* **228**, 8203–8213.
- VIRÉ, A., KRASNOV, D., BOECK, T. & KNAEPEN, B. 2011 Modeling and discretization errors in Large Eddy Simulations of hydrodynamic and magnetohydrodynamic channel flow. *J. Comp. Phys.* **230**, 1903–1922.
- VON HARDENBERG, J., PARODI, A., PASSONI, G., PROVENZALE, A. & SPIEGEL, E. 2008 Large-scale patterns in Rayleigh-Bénard convection. *Phys. Lett. A* **372** (13), 2223–2229.
- VOROBEOV, A., ZIKANOV, O., DAVIDSON, P. A. & KNAEPEN, B. 2005 Anisotropy of magnetohydrodynamic turbulence at low magnetic Reynolds number. *Phys. Fluids* **17** (12), 125105, arXiv: <https://doi.org/10.1063/1.2140847>.
- YAKHOT, V. 1992 4/5 Kolmogorov law for statistically stationary turbulence: Application to high-Rayleigh-number Bénard convection. *Phys. Rev. Lett.* **69**, 769–771.
- YEUNG, P. K. & ZHOU, Y. 1997 Universality of the Kolmogorov constant in numerical simulations of turbulence. *Phys. Rev. E* **56**, 1746–1752.
- ZÜRNER, T., SCHINDLER, F., VOGT, T., ECKERT, S. & SCHUMACHER, J. 2019 Combined measurement of velocity and temperature in liquid metal convection. *J. Fluid Mech.* **876**, 1108–1128.
- ZWIRNER, L., KHALILOV, R., KOLESNICHENKO, I., MAMYKIN, A., MANDRYKIN, S., PAVLINOV, A., SHESTAKOV, A., TEIMURAZOV, A., FRICK, P., SHISHKINA, O. & ET AL. 2020 The influence of the cell inclination on the heat transport and large-scale circulation in liquid metal convection. *J. Fluid Mech.* **884**, A18.